Dust and Gas in NGC3627

Dust and Gas in NGC3627 Using Observations from SCUBA-2

By

Jonathan H. Newton, B.A.

A Thesis

Submitted to the School of Graduate Studies

in Partial Fulfilment of the Requirements

for the Degree

Master of Science

McMaster University

MASTER OF SCIENCE (2014)   McMaster University

(Physics and Astronomy)   Hamilton, Ontario

TITLE: Dust and Gas in NGC3627 Using Observations from SCUBA-2

AUTHOR: Jonathan Newton, B.A. (Western Kentucky University)

SUPERVISOR: Christine D. Wilson

NUMBER OF PAGES: xii, 92

Abstract

Saw some dust and wanted to do something about it!

To my family and Poly.

Acknowledgements

When life looks like easy street, there is danger at your door... -Robert Hunter

Thank Chris and group members of course. Don't forget Christian!

Table of Contents

List of Figures

List of Tables

Chapter 1

Introduction

1.1 The Physical Processes of Star Formation

Star formation is one of the fundamental processes in astrophysics that affects not just stellar and planetary formation but also dictates the behavior in galaxy formation and evolution (Kennicutt & Evans, 2012). The study of star formation itself can be broken into several areas such as: the processes that trigger collapse and how the collapse behaves, dictating how and what type of stars can form from a given region or cloud, or how the inflow of new material can alter current star forming environments. These different sub-branches of star formation are conveniently sorted into hierarchal schemes that range from Mpc scales seen in gas accretion from the intergalactic medium, to properties of accretion disks on scales of the order $R_\odot$ or AU(Kennicutt & Evans, 2012). In this body of work we focus on the physical properties of the dust and abundance of gas in the giant molecular cloud (GMC) phase of star formation prior to stellar collapse or fragmentation. However based on the resolution of

our target galaxy, we will not be able to examine individual GMCs instead we will need to focus our work on giant molecular associations (GMAs).

1.1.1 GMC Formation

After intergalactic gas has accreted into a host galaxy, it condense and lead to the formation of molecular clouds (Kennicutt & Evans, 2012). The dominant process of GMC formation is divided between two camps, either a "bottom-up" or "top-down" formation scenario (McKee & Ostriker, 2007). The bottom-up scenario consists of small clouds of cold HI coagulating to eventually form a GMC (Field & Saslaw, 1965; Kwan, 1979). The major concern with the bottom-up scenario is if we include heating mechanisms in the cloud, coagulation will cease before the observed masses are reached (McKee & Ostriker, 2007). In fact, the time scales required to form a cloud typical of those we observe would take around 10^8 years to accumulate a minimum of 10^5 $M_\odot$, which is much greater than the expected GMC lifetime (McKee & Ostriker, 2007).

The alternative formation scenario, top-down, postulates the GMC formation comes from instabilities in the diffuse ISM causing the clouds to collapse from their surrounding medium (McKee & Ostriker, 2007). Two main instabilities are thought to be responsible for the collapse. The first type of instability is a Parker instability, which involves distortion of magnetic field lines in the mid-plane of the galaxy, and at these distortions gas will begin to accumulate (Parker, 1966; Dobbs et al., 2013). The second instability responsible for collapse comes can be determined by the amount of rotational shear present

(McKee & Ostriker, 2007). If a strong rotational shear is present, such as in the inter-arm region of a spiral galaxy, then the accumulation of gas will be due to its shearing as it moves through the disk of a galaxy in a process known as swing amplification (McKee & Ostriker, 2007; Dobbs et al., 2013). If no rotational shear is present, such as the inner regions of a galaxy or spiral arms, then the collapse can be attributed to a magneto-Jeans instability which will remove the angular momentum responsible for the rotational shear through magnetic fields in order for the normal Jeans instability to occur (Elmegreen, 1987; Kim & Ostriker, 2001).

1.1.2 Molecular Hydrogen Formation

Regardless of either collapse or coagulation, molecular hydrogen is being formed inside the cloud. The formation of molecular hydrogen can be summarized using either the two body reaction, three body reaction, formation using a free electron or proton, or surface formation (Krumholz, 2014). The two body formation scenario is the simplest reaction using two hydrogen atoms to produce molecular hydrogen,

$$H + H \longrightarrow H_2 \tag{1.1}$$

However the two body formation is not the major mechanism in the formation of H_2 due to the requirement of a forbidden photon that arises from the combination of hydrogen atoms in the ground state (Gould & Salpeter, 1963). If one of the hydrogen atoms is excited, the transition can occur and

3

molecular hydrogen is formed, but the amount of excited hydrogen atoms in the temperature ranges typical of the cold and warm phases of the ISM are expected to be nearly nonexistent (Krumholz, 2014).

The second formation scenario listed, the three body formation, involves three hydrogen atoms coming together to form molecular hydrogen with a spare hydrogen atom shown in reaction,

$$3\,\mathrm{H} \longrightarrow \mathrm{H}_2 + \mathrm{H}. \tag{1.2}$$

The required density for the three body formation to occur is on the order of $10^8\ \mathrm{cm}^{-3}$ (Palla et al., 1983; Abel et al., 1997), while the typical GMC density is on the order of $300\ \mathrm{cm}^{-3}$. The disparity between these densities eliminates any possibility of this being the primary mechanism to form molecular hydrogen in galaxies today.

An alternative to the two or three body reactions uses either an electron or proton to ionize the hydrogen forming either H^- or H_2^+ (Krumholz, 2014). The chemical reaction involving an electron is shown in reaction 1.3, and the reaction utilizing a proton is shown in reaction 1.4

$$\mathrm{H} + e \longrightarrow \mathrm{H}^- + h\nu$$
$$\mathrm{H}^- + \mathrm{H} \longrightarrow \mathrm{H}_2 + e \tag{1.3}$$

$$\mathrm{H} + \mathrm{H}^+ \longrightarrow \mathrm{H}_2^+ + h\nu$$
$$\mathrm{H}_2^+ + \mathrm{H} \longrightarrow \mathrm{H}_2 + \mathrm{H}^+ \tag{1.4}$$
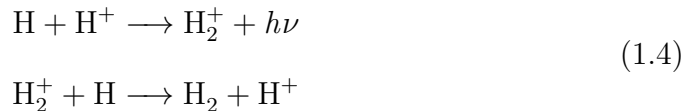
The main limitation of the free electron/proton formation mechanism is an undersupply of free electrons and protons. Typical Milky Way conditions show that regions >1 cm^{-3} have free electron and proton densities $<10^{-4}$ cm^{-3} (Wolfire et al., 2003). Secondly, the H$^-$ ion in reaction 1.3 is more likely to interact with a stray photon than an electron resulting in the ion returning to the atomic state (Glover, 2003). While we observe singly ionized hydrogen regions, HII regions, only a small fraction of the region will successfully produce molecular hydrogen.

While the free electron/proton formation method is suspected to be the primary H$_2$ catalyst in the early universe (Herbst et al., 2005), at low redshifts the formation of molecular hydrogen on the surface of dust grains is the dominant mechanism of formation (Krumholz, 2014). The surface formation of molecular hydrogen will occur when a hydrogen atom strikes a dust grain and successfully sticks to the grain. The hydrogen will then interact with another hydrogen atom to form H$_2$ and be ejected from the dust particle after the reaction has occurred (Pirronello et al., 1997). The same process occurs on the dust grain as the two body formation in the gas phase, but the dust grain will act as a medium to absorb the energy that would create the forbidden photon (Krumholz, 2014).

With a dominant mechanism for molecular hydrogen formation, a reaction rate can be defined based on the cross section of the grain, Σ_{gr}, a striking probability dependent on the temperature of the observed dust, S(T), the probability of molecular hydrogen forming on the grain, ϵ_{H_2}, the density of free hydrogen in the GMC, n_H, and the density of hydrogen attached to the grain

surface, n_{H0} (Krumholz, 2014). Scaling this with the integrated collisional probability of a Maxwellian gas, the reaction rate is determined to be

$$\frac{dn_{H_2}}{dt} = \frac{1}{2} \left(\frac{8k_b T}{\pi m_H} \right)^{\frac{1}{2}} \Sigma_{gr} S\left(T\right) \epsilon_{H_2} n_H n_{H_0} \tag{1.5}$$

where k_b is the Boltzmann constant, T is the temperature, and m_H is the mass of the hydrogen atom. Equation 1.5 is often simplified to

$$\frac{dn_{H_2}}{dt} = \mathcal{R}_{gr} n_H n_{H_0} \tag{1.6}$$

by introducing a variable known as the formation rate, $\mathcal{R}_{gr}$, that is constrained using the column densities of CI, CII, HI, H_2. Using the column densities of CI and CII to determine a reaction rate is built around examining their ratios and the mechanisms that convert from ion to atom and atom to ion. The neutralization of CII involves its interaction with polycyclic aromatic hydrocarbons, and the ionization of C takes place by interacting with far-ultraviolet (FUV) photons (Wolfire et al., 2008). The FUV intensity will also dictate the amount of disassociation of H_2 into H, and by balancing the amount of CI and CII with the amount of H and H_2, the FUV intensity can be determined as well as the amount of H_2 being produced (Wolfire et al., 2008). Typical reaction rates for the Milky Way have been found to be $3 \times 10^{-17} \text{cm}^3 \text{s}^{-1}$ (Jura, 1975; Gry et al., 2002; Wolfire et al., 2008).

1.1.3 Dissociation of Molecular Hydrogen

When the molecular hydrogen has formed, it is still susceptible to photodissociation from FUV photons. The energy required for a single photon to break the bonds of molecular hydrogen is 14.5 eV (Krumholz, 2014). Conveniently, this is also enough energy to excite atomic hydrogen, so photodissasociation using a single photon is highly unlikely due to the abundance of HI in the ISM (Krumholz, 2014). However, a photon with an energy of 11-13.6 eV will not be able to excite atomic hydrogen, but will be able to excite the molecular hydrogen to its first and second excitation levels, the Lyman and Werner bands respectively. The excited H_2 will eventually settle via photon emission to its ground state with a finite probability of returning to two hydrogen atoms rather than maintaining its molecular state (Krumholz, 2014).

A dissociation rate, ζ_{diss}, can be obtained by scaling the total excitation rate, ζ_{exc}, by the fraction of excited hydrogen molecules that will settle to an atomic ground state (Krumholz, 2014). The total excitation rate is found by summing each individual excitation from the ground state e.g. $\zeta_{exc,0-1}$, $\zeta_{exc,0-2}$. In the Milky Way's diffuse ISM, the interstellar radiation field is 6-9x10^{-14} erg cm^{-3} over the range of 6-13.6 eV resulting in $\zeta_{exc} \approx 3 \times 10^{-10} \text{s}^{-1}$ (Draine, 2011). The expected fraction of H_2 to disassociate is between 0.11 and 0.13 resulting in $\zeta_{diss} \approx 4 \times 10^{-11} \text{s}^{-1}$ (Draine, 2011). Equating the formation and dissociation rates and then solving for a molecular hydrogen vs atomic hydrogen ratio gives

$$\zeta_{diss}n_{H_2} = \mathcal{R}n_{H_0}n_H$$

$$\frac{n_{H_2}}{n_H} = \frac{\mathcal{R}n_{H_0}}{\zeta_{diss}}$$

$$= 8 \times 10^{-6} \left(\frac{4 \times 10^{-11}s^{-1}}{\zeta_{diss}} \right) \left(\frac{n_{H_0}}{10cm^{-3}} \right) \tag{1.7}$$

(Krumholz, 2014). From equation 1.7 we can see, in the diffuse medium, atomic hydrogen is far more abundant than molecular hydrogen, as expected.

However, as the density of the gas increases via collapse or coagulation, the optical depth will also increase, limiting the amount of FUV photons able to penetrate into the core of the cloud, a process known as shielding (Draine, 2011). This shielding will decrease the value of ζ_{diss} which will increase the n_{H_2}/n_H ratio in equation 1.7. The increase in the molecular to atomic hydrogen ratio signifies the accumulation of molecular gas reservoirs. The molecular gas build up will lead to fragmentation within the cloud, and will eventually lead to forming stars.

1.2 Determining the H$_2$ Abundance

From the previous section, the formation of molecular hydrogen will result in the energy released during creation being absorbed by a dust grain rather than through emission resulting in H$_2$ creation being a dark process (§1.1.2). Furthermore, since the molecule is made of two hydrogen atoms, an extreme symmetry and low mass will negate any permanent dipole effects making low energy rotational transitions nonexistant (Bolatto et al., 2013; Kennicutt & Evans, 2012). The high symmetry and low mass does not mean H$_2$ is unex-

citable, but the temperatures required to excite molecular hydrogen are (T $\gtrsim$ 100K) above the temperature of a typical GMC (Bolatto et al., 2013). Also the settling of H_2 will more often than not result in the molecule separating into two hydrogen atoms (§1.1.3). For our purposes, we can consider molecular hydrogen a dark molecule requiring special treatment to determine the amount present.

Calculating the amount of molecular hydrogen in a system can be performed in several ways, and for the purpose of extragalactic sources they all involve using a molecular tracer to determine the amount of H_2 present. The molecule most commonly used in extragalactic studies is CO due to its abundance and ability to be easily observed (Bolatto et al., 2013). Other tracers that have been used are CO's photodissociated counterpart, CII, in order to trace regions that have little to no CO emission (Madden et al., 1997), and molecules such as OH that have been used in the past but have been limited to Milky Way targets (Barrett, 1964). The amount of CO can then be converted to H_2 using a conversion factor (either X_{CO} or α_{CO} depending on whether the final solution is in terms of column density or surface density). Typical values for X_{CO} in normal spiral galaxies tend to be around 1-4$\times10^{20}$ cm^{-2} (K km s^{-1})$^{-1}$, and a commonly used value for the Milky Way is 2×10^{20} cm^{-2} (K km s^{-1})$^{-1}$ (Bolatto et al., 2013). Values of α_{CO} for nearby extragalactic sources have shown a mean value of 3.1 M$_\odot$ pc^{-2} (K km s^{-1})$^{-1}$ which is slightly lower than the assumed Milky Way value of 4.4 M$_\odot$ pc^{-2} (K km s^{-1})$^{-1}$ (Sandstrom et al., 2013).

1.2.1 Methods for Determining CO-to-H_2 Conversion Factor

Several methods are available to determine the conversion factor for extragalactic sources, and each has its own caveats. One common method used to determine a conversion factor is to use the virial nature of GMCs (Bolatto et al., 2013). This method works best for well defined clouds; however in the case of more distant nearby galaxies, the issue of whether or not GMAs display the same virialization as their constituent GMCs can limit concrete results (Bolatto et al., 2013). The second caveat of using the virial mass to determine a conversion factor is the method will only trace CO bright regions. Tracing only CO bright regions has led this method to results that show no dependence between the conversation factor and metallicity, while other methods display a negative correlation between the conversion factor and metallicity (Bolatto et al., 2013). The mechanism discrediting the zero dependence is believed to be due to weak dust shielding present in the system and corresponds to a low metallicity. The poor shielding will allow the CO to be dissociated resulting in large amounts of molecular hydrogen traced by ionized and atomic carbon gas instead of CO (Bolatto et al., 2013). While the virial method is suitable for determining conversion factors within CO bright regions, excluding any low metallicity regions will underestimate the total amount of H_2 present in the system as well as skew any possible relations of the conversion factor with metallicity (Bolatto et al., 2013).

A second method to ascertain a conversion factor is to incorporate observations of isotopologues of CO that are optically thin, commonly ^{13}CO (Bolatto et al., 2013). The temperature, density, and column or surface density of

the ^{13}CO can be used to restrict the possible outcomes of the physical conditions of the GMC or GMA being examined. The main problem with using this method is the degeneracy between the temperature and density of CO emission such that hot low dense can resemble cool dense emission (Rosenberg et al., 2014). This method also shares the same problem as the virial technique in that it only probes CO bright regions of the target leaving any CO-faint H_2 gas untraced (Bolatto et al., 2013). The issue of CO-faint molecular hydrogen has been examined using the photodissociated tracer of CO, CII, as the isotopologue instead of ^{13}CO. The CII ion was used as a tracer of molecular hydrogen in dwarf galaxies and was able to reveal large reservoirs of self-shielding H_2(Madden et al., 1997).

The third way to determine a CO-to-H_2 conversion factor is by incorporating the emission from dust to determine the amount of molecular gas present. This method assumes that the gas is well mixed and has a constant ratio of dust mass to gas mass present in the galaxy (Leroy et al., 2011), which has been shown to be true for the Milky Way (Boulanger et al., 1996). A suitable conversion factor is found by solving

$$
\begin{aligned}
\delta_{GDR}\Sigma_{dust} &= \Sigma_{H_2} + \Sigma_{HI} \\
&= \alpha_{CO}I_{CO} + \Sigma_{HI}
\end{aligned}
\tag{1.8}
$$

where Σ_{dust}, Σ_{H_2}, and Σ_{HI} are the respective surface densities in $M_\odot$ pc^{-2}, I_{CO} is the CO line intensity, α_{CO} is the conversion factor in $M_\odot$ pc^{-2} K^{-1} km^{-1} s, and δ_{GDR} is the total mass of the gas divided by the total mass of the dust known as the gas-to-dust ratio (Leroy et al., 2011; Sandstrom et al.,

2013). In equation 1.8, we can measure Σ_{dust}, Σ_{HI}, and I_{CO} leaving only the conversion factor and gas-to-dust ratio free to vary. An appropriate α_{CO} value will generate a molecular gas mass that produces a constant gas-to-dust ratio over the galaxy being studied. This method been carried out extensively by Sandstrom et al. (2013) on kpc scales on nearby galaxies as well as on both of the Magellenic clouds by Leroy et al. (2011).

Determining a conversion factor in this manner provides the capability to trace the CO faint regions of a target unlike the previous methods (Israel et al., 1996). Despite this advantage over the other two methods, using equation 1.8 leaves any gas not associated with atomic hydrogen to be treated as H_2. This is shown in equation 1.8 given that the total amount of gas is the product of δ_{GDR} and Σ_{dust} and the amount of molecular H_2 is the amount of gas that is not atomic hydrogen. This will affectively increase the conversion factor and the overall amount of molecular hydrogen reported(Bolatto et al., 2013). Another caveat of this method rests with the assumption of a constant dust-to-gas ratio (Bolatto et al., 2013). Issues such as the gas-to-dust ratio's dependence with metallicity (Draine et al., 2007) can render this assumption null if not treated properly. Nevertheless, the agreement of conversion factors between the dust based method and other methods used for more local targets suggests that any gas present that has been incorrectly assumed to be H_2, and local fluctuations in metallicity of the target galaxy have very little effect on the final results (Bolatto et al., 2013).

1.3 Determining Dust Mass

Approximating a conversion factor using dust emission requires a knowledge of the amount of dust present in our system to determine a gas-to-dust ratio. Given that a significant portion of the dust mass lies within the cold phase we can calculate a dust mass using a modified blackbody fit over the cold portion of the dust's spectral energy distribution (SED) (Galametz et al., 2012). A slight modification needs to be introduced to our blackbody resulting in what is known as a greybody or modified blackbody (MBB). The modification is necessary because the dust does not absorb and re-emit all of the light incident on its surface. If we assume an isolated optically thin medium ($\tau_\nu \ll 1$) with a blackbody source function, $B_\nu(T)$, the radiative transfer equation can be written as

$$I_\nu = \left(1 - e^{-\tau}\right) B_\nu\left(T\right), \tag{1.9}$$

and simplified using a first order Taylor expansion with $\tau_\nu \ll 1$ to get

$$I_\nu = \tau_\nu B_\nu\left(T\right) \tag{1.10}$$

The optical depth can be expanded to incorporate the surface density of the dust, Σ_{dust}, as

$$\tau_\nu = \kappa_\nu \Sigma_{dust} \tag{1.11}$$

The dust emissivity cross-section per unit mass is represented by κ_ν and is often referred to as the opacity. It is important to note that the opacity will reflect

the chemical makeup and grain structure of the dust, but will not indicate the grain size (Abergel et al., 2013). The behavior of the opacity has been well fit with a power law such that opacity shows a dependence with the frequency of the observed emission (Hildebrand, 1983). The opacity is typically written as

$$\kappa_\nu = \kappa_{\nu,0} \left(\frac{\nu}{\nu_0} \right)^\beta \tag{1.12}$$

where ν_0, is a reference frequency, κ_ν is a reference opacity based on the reference frequency, and β the dust emissivity index. Values for κ_ν have been calculated for several models of varying dust compositions and can range from 0.2 to 2 m^2 kg^{-1} over the wavelengths used to model the cold component (100μm–850μm)(Li & Draine, 2001). The emissivity index has commonly been fit between ranges of 1.0 to 2.0 suggested from laboratory experiments (Walcher et al., 2011). However, with the influx of Herschel data the ability to fill in the sub-millimeter portion of the SED between 100μm and 500μm has allowed the emissivity index to be determined based on observations and have shown a range from 1 to 2.5 (Galametz et al., 2012). It should be noted that the lower limit of β=1 is a hard cutoff due to limits determined by the Kramers-Kronig relationship in the optically thin case(Li, 2005), but in extreme instances when the dust becomes optically thick β will approach 0.

With the opacity well defined, substituting equation 1.12 into equation 1.11 and then into the original equation for the specific intensity of our MBB, equation 1.10, gives the formula for the specific intensity of a greybody as

$$I_\nu = \Sigma_{dust}\kappa_{\nu,0} \left(\frac{\nu}{\nu_0}\right)^\beta B_\nu(T) \tag{1.13}$$

Since we measure the flux of our target, it is useful to convert from the specific intensity to the flux using

$$F_\nu = \pi I_\nu \left(\frac{r}{D}\right)^2 \tag{1.14}$$

given the target is a uniform sphere with radius, r, and distance, D (Rybicki & Lightman, 1986). Substituting equation 1.14 into the greybody equation, 1.13, gives

$$S_\nu = \frac{\Sigma_{dust}\pi r^2}{D^2}\kappa_\nu \left(\frac{\nu}{\nu_0}\right)^\beta B_\nu(T). \tag{1.15}$$

Converting from surface density to overall mass is done using the relationship between mass and surface density of M=Σ*Area where the targets projected area πr^2. This gives a final modified blackbody equation of

$$S_\nu = \frac{M_dust}{D^2}\kappa_\nu \left(\frac{\nu}{\nu_0}\right)^\beta B_\nu(T). \tag{1.16}$$

The dust mass can be solved from equation 1.16 by either fitting the mass, temperature, and possibly the emissivity index. The fitted mass will act as a normalizing factor for the SED and correspond with the mass associated at the peak flux. Using the fitted dust mass should be used cautiously due to a sensitivity in mass with temperature fluctuations (Draine et al., 2007). An

alternative to using the fitted mass is to isolate the mass from equation 1.16 to get

$$M_{dust} = \frac{S_\nu D^2}{\kappa_\nu B_\nu \left(T\right)} \left(\frac{\nu}{\nu_0}\right)^{-\beta} \qquad (1.17)$$

and use the parameters returned from fitting. This equation is best used with a longer wavelength observation that will explore the Rayleigh-Jeans tail of the modified blackbody. This portion of the SED will see less of a dependence in the mass and temperature fluctuations (Draine et al., 2007). The main concern with both methods to ascertain the mass arises from fitting both the temperature and dust emissivity index and their strong anti-correlation (Galametz et al., 2012; Tabatabaei et al., 2014). A common method to help break the degeneracy is to fix emissivity index to a reasonable value based upon the opacity model (Tabatabaei et al., 2014).

1.4 NGC 3627

In this thesis, we are using the new SCUBA-2 instrumentation on the JCMT taken from the NGLS, which observes both 450μm and 850μm emission simultaneously. Utilizing multiple 60 minute scans in high quality weather we can better constrain the emissivity index in our fits, as well as increase the resolution compared to previous work. With these new observations we can better fit an SED and determine a more reliable dust mass to explore the amount of molecular gas present. To take full advantage of the benefits

of SCUBA-2, we have selected the target NGC3627 for its relatively small angular size, pronounced spiral features, and relatively large flux.

NGC 3627 is the most prominent member of the interacting trio of galaxies called the Leo triplet (NGC 3623, NGC 3627, and NGC3628). An optical image is shown in Figure 1.1 while the data we used can be seen in sections §2.2 and §2.3. The interaction between NGC 3627 and NGC 3628 has been well documented via HI emission in the form of a large HI debris tail extending from NGC 3628 in the direction of NGC 3627 (Rots, 1978; Haynes et al., 1979). The interaction between these galaxies has resulted in a high star formation activity of over 1.7 $M_\odot$ yr^{-1} (Calzetti et al., 2010), making NGC 3627 a prime candidate to study the current star forming conditions. The morphology of NGC 3627 is that of a barred spiral (SABb) with an inclination of 60° (Reuter et al., 1996) at a distance of 9.4 Mpc determined by Cepheid variable observations (Freedman et al., 2001). Furthermore, the strong spiral arm features are unique to this galaxy in that speculation exists they are not contained within the plane of the galaxy. Which has been supported by magnetic field lines traced by dust polarization that do not trace the spiral structure in the southeastern bar end (Soida et al., 2001) and CO observation with a bimodal emission features in the velocity space over the southeastern bar end(Dumke et al., 2011).

NGC 3627 is a member of the Spitzer Infrared Nearby Galaxies Survey (SINGS) (Kennicutt et al., 2003) and has been observed throughout the electromagnetic spectrum. ^{13}CO observations by Watanabe et al. (2011) have shown that a majority of the star formation is occurring in the bar ends of
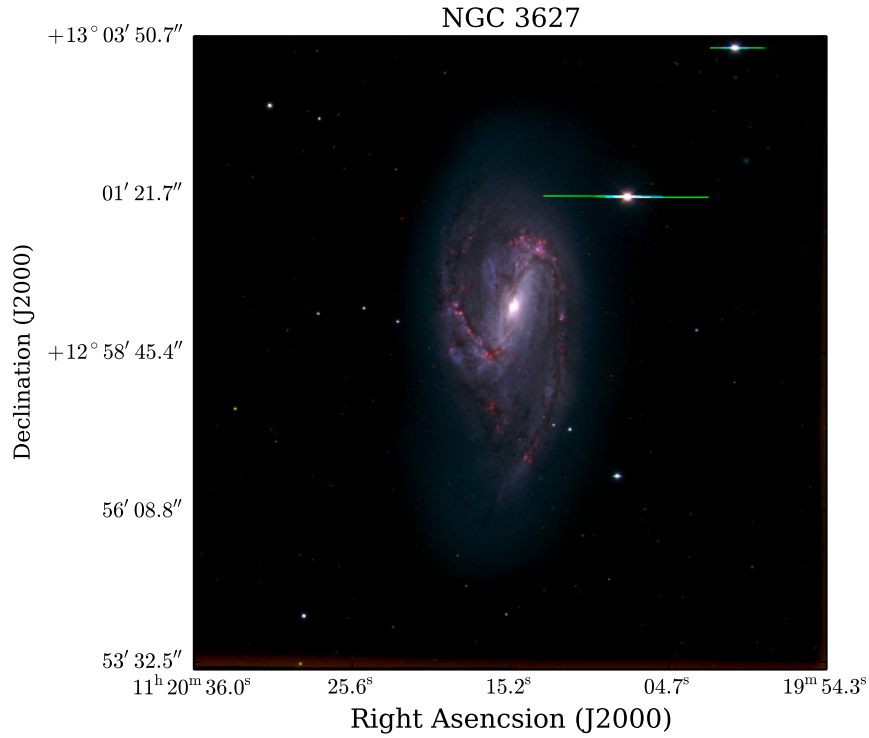
Figure 1.1: Optical composite image of NGC3627 made the SINGS 5th enhanced data release (Kennicutt et al., 2003). Blue areas represent the B band, green areas represent V band and red areas show the Hα band. Component images were retrieved from NED.

the galaxy. This information corresponds with Warren et al. (2010) showing the star formation efficiency being highest in the bar ends. Warren et al. (2010) also shows the ISM of the galaxy to be dominated by molecular gas, with dense warm gas dominating the emission at the bar ends, nucleus and a bright region located beneath the southwestern spiral arm, and more diffuse and cooler molecular gas outside of these regions. The atomic gas is located primarily in the spiral arms with little to no emission in the nucleus of the galaxy. A mean conversion factor of α_{CO}=1.2 M$_\odot$ pc^{-2} (K km s^{-1})$^{-1}$ was found by Sandstrom et al. (2013) using the dust method (§1.2.1). An HI mass was given as 8.18×10^8 M$_\odot$ (Walter et al., 2008), and a corresponding H$_2$ mass was calculated as 5.79×10^9 M$_\odot$ (Kennicutt et al., 2003), and a stellar mass of 2.8×10^{10} M$_\odot$ (Skibba et al., 2011).

The dust emission of NGC 3627 follows the same trend as the CO emission with the brightest regions at the bar ends, nucleus, and a bright region below the southwest bar end. The southeastern spiral arm shows some knotted features in the dust emission. Global values for the cold and warm components of the SED were fit by Galametz et al. (2012) and reveal dust temperatures of T$_W$=55.8±5.6 K and T$_C$=20.2±1.4 K for the warm and cold components, respectively, with a best fit emissivity index of β=2.3±0.2 and a total dust mass of 7.82×10^7 M$_\odot$.

This thesis will explore the properties of dust emission from NGC3627 by exploring its SED using new observations from SCUBA-2 in order to increase the help the mass and dust emissivity index at a higher resolution in order to build on the work of Galametz et al. (2012). Furthermore, we can look use

our SED derived dust masses to determine the overall amount of molecular gas present in the galaxy parameters while gaining insight into the dust-to-gas ratio and conversion factor for this galaxy using the methods outlined by Leroy et al. (2009) and Sandstrom et al. (2013). The information in this thesis is arranged as follows: Chapter 2 will describe the data reduction and properties of the SCUBA-2 data and any ancillary data, Chapter 3 will describe the SED fitting method, Chapter 4 will go over the method to determine a dust-to-gas ratio, and Chapter 5 will consist of summarizing our findings.

Chapter 2

Observations and Data Preparation

2.1 SCUBA-2

The Submillimetre Common-User Bolometer Array 2 (SCUBA-2) was designed to decrease the observing time of the sub-millimeter sky relative to its predecessor SCUBA (Holland et al., 2013). This would benefit the community by allowing for rapid data acquisition in the submillimeter regime of the electromagnetic spectrum, at the 450μm and 850μm bands in particular. Prior to SCUBA-2, other bolometer cameras such as LABOCA, BOLOCAM and SHARC-II were limited to less than 100 pixels, while the new SCUBA-2 has been able to incorporate over 10,000 pixels in its design and effectively reduce the required observing time (Chapin et al., 2013). Increasing the amount of pixels by a factor of 100 was possible by the advent of new technology such as high precision micromachining, superconducting transition edge sensors, and superconducting quantum interference device amplifiers (SQUIDs) (Holland et al., 2013).

The observations of NGC3627 were taken from the Nearby Galaxies Legacy Survey's (NGLS) initial science images using SCUBA-2 from December 29, 2011 to January 21, 2012, and consist of 24 18′ by 18′ scans taken in grade 3 weather or better ($0.08 < \tau < 0.12$) with observations centered at 450μm and 850μm emission with a 32μm and 85μm bandpass respectively. 16 of the 24 scans were deemed useable, and whether or not an observation was deemed worthwhile was determined by factors such as the behavior of the image background or whether the image was flagged during observing to be unusable. The observations of NGC3627 were taken using a daisy scanning pattern to help remove any random noise by introducing crossing points. The scanning speed of the JCMT was 150″/second in order to negate any drifting effects seen from the instrument or sky (Chapin et al., 2013).

2.2 Image Creation and Properties

For any imaging process to be successful, the final image needs to have a limited white noise (Chapin et al., 2013). White noise in the sense of our bolometer observations arises from thermal variations in the instrument and atmosphere during data acquisition. The random noise is minimized through scanning methods and during image processing (Chapin et al., 2013). To create the final SCUBA-2 data products, we use the Submillimetre User Reduction Facility (SMURF) procedure MAKEMAP. This procedure reduces the noise of the observations while maintaining the source's emission by incorporating a combination of principal component analysis and a maximum likelihood analysis (Chapin et al., 2013). Both of these methods have proven useful in

reducing bolometer data on their own, but due to the size of raw SCUBA-2 data, either method on its own would result in extreme run times or the process becoming resource intensive (Chapin et al., 2013).

MAKEMAP breaks down the image creation into several steps performed in iteration in order to successfully reduce any background noise (Chapin et al., 2013). The raw data is modeled by

$$b_i(t) = f\left[e_i(t) * a_i(t) + g_i * n_c(t) + n_f(t) + n_r(t)\right] \qquad (2.1)$$

such that $b_i(t)$ is the ith bolometer output at time t, f is a scaling factor determined from flat field calibrations, $e_i(t)$ is the extinction at time t for the ith bolometer, $a_i(t)$ is the astronomical signal for ith bolometer at time t, $g_i * n_c(t)$ is the noise due to the product of the common mode and gain, $n_f(t)$ is the low-frequency noise, and $n_r(t)$ is the random noise (Chapin et al., 2013).

The steps used in MAKEMAP are designed so they can estimate each noise component of the bolometer signal. The COM and GAI steps estimate a common mode signal by fitting the average time-series of each bolometer observation. The next step is EXT, which is used to apply the measured extinction corrections. Following EXT is FLT to apply high- and low-pass filters to remove any noise features not removed in the COM and GAI filtering. After the high- and low-pass filters, the AST step is performed. AST converts the data from a time series to an image and detects sources to be removed from reduction. The sources removed during this portion of MAKEMAP are intended to be astronomical in nature. The final step is NOI which determines the noise in the gridded map after each step has been performed and is calcu-

lated by isolating the white noise component in equation 2.1. A convergence check is then issued based on the magnitude of change in each pixel from the previous map and the current version. If the check fails, the COM, GAI, EXT, and FLT values are recalculated using the AST information obtained from the previous iteration, and the process is repeated until the convergence values are met or the maximum number of iterations have been carried out (Chapin et al., 2013).

In our production of maps, we used the configuration file dimmconfig_bright _compact.lis and altered the AST and FLT sections of the image creation by introducing a mask made from Herschel's 250μm map. The purpose of the mask was to exclude the target from interfering with the noise minimization as well as prohibit any emission from the galaxy to be significantly altered during image production. The filter size of the high-pass filter was also modified, and an appropriate value was determined to be $175''$. We determined an appropriate high-pass filter size by running a large range of filters from $100''$ to $300''$ and inspecting the total recovered flux of NGC3627. A plot of the returned flux values can be seen in Figure 2.1. A good filter would not show any significant decrease in flux compared to the 350μm or 500μm. This requirement removes any filters greater than $200''$. Given the flux was nearly constant with filters less than $200''$, we chose an appropriate filter size by examining the structure that was returned, in particular how well the spiral arms were recovered for the 850μm, and how well the disk was preserved in the 450μm. The spatial effect of the filters can be seen in Figure 2.2 for the 450μm and Figure 2.3 for the 850μm. The maps were returned from MAKEMAP in units of pW with a pixel size of $2''$ by $2''$ for both the 450μm and 850μm.
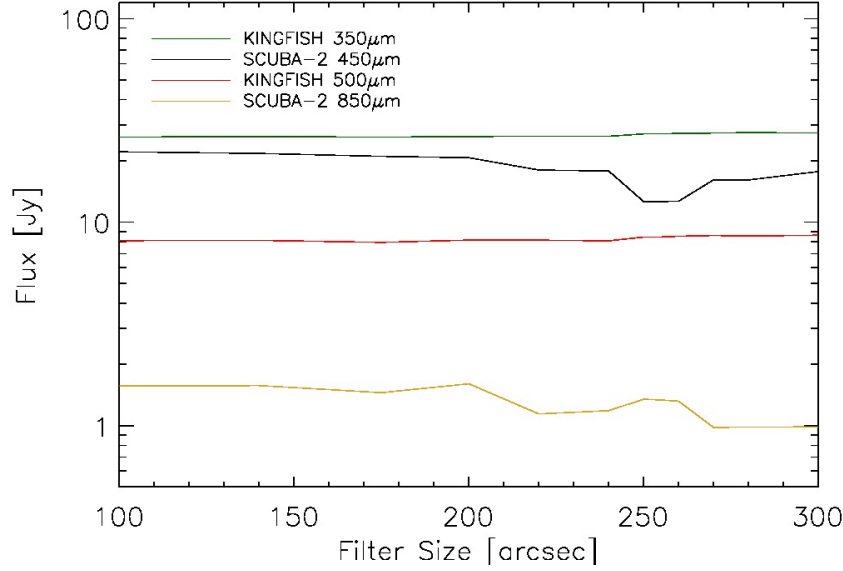
Figure 2.1: Returned flux values for NGC3627 with varying high-pass filter sizes. The KINGFISH fluxes have been been processed using the fakesource process, §2.4.2

The finalized 450μm image was then re-gridded down to a $4''$ by $4''$ pixel grid, and flux calibration values of 491000 and 4710 were applied to convert from pW to mJy/beam and mJy/square arcsecond, respectively. The 850μm maps were re-gridded to an $8''$ by $8''$ pixel size and used flux calibration values of 537000 and 2340 for mJy/beam and mJy/square arcsecond. The $4''$ and $8''$ pixels corresponded to a 180pc and 360pc size scale for our target, NGC3627. To simplify the analysis, the images are also converted to Jy/pixel. The 450μm and 850μm images are shown in Figures 2.4 and 2.5. The calibration values used are the default flux calibration factors that are determined from our calibrator source, Uranus. The overall noise in the final image can be seen in Table 2.1.
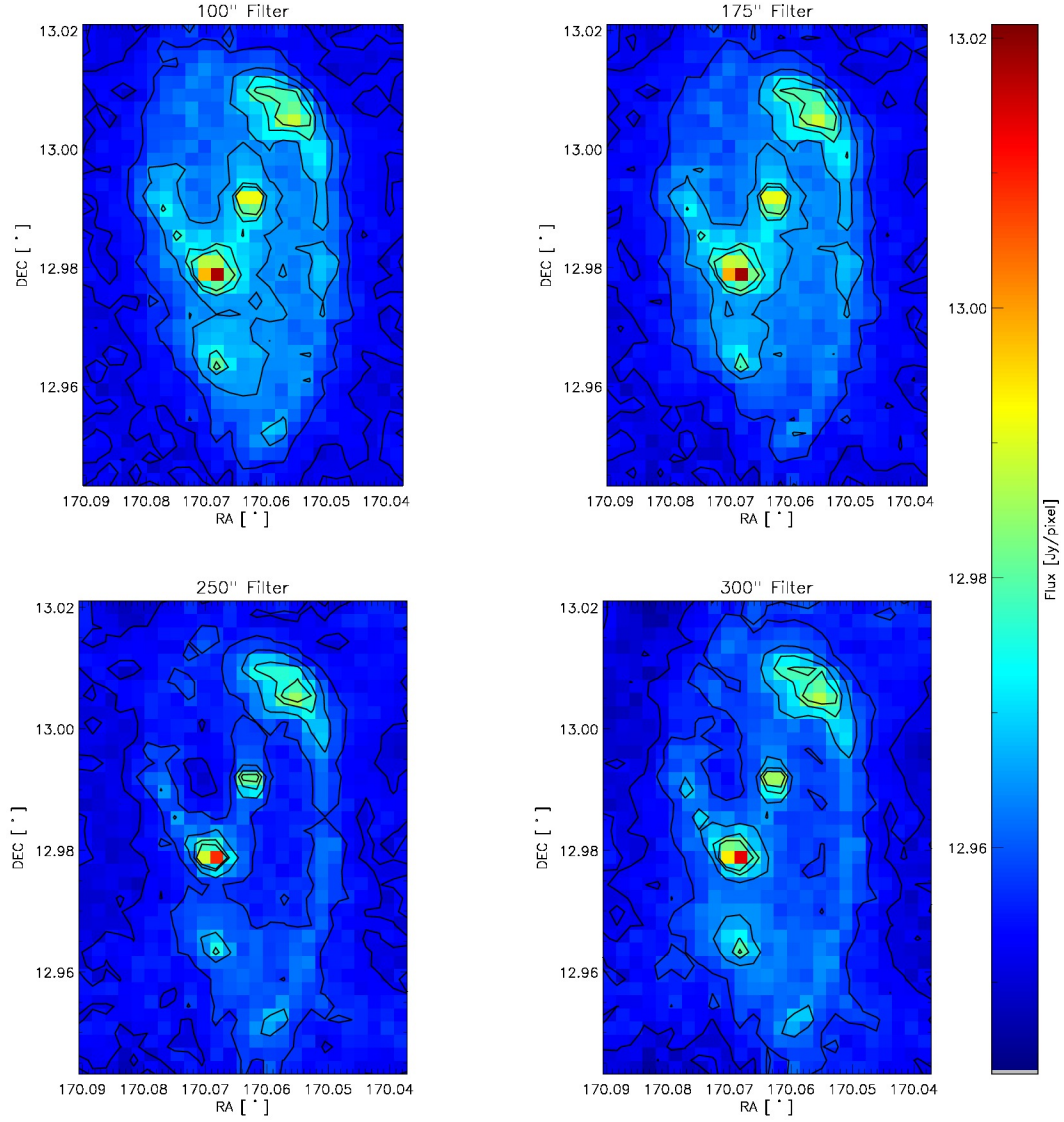
Figure 2.2: Four 450μm maps of NGC3627 using varying high-pass filter sizes. The contours shown are for 0.0, 0.02, 0.05, 0.08 and 0.1 Jy/pixel for each image.
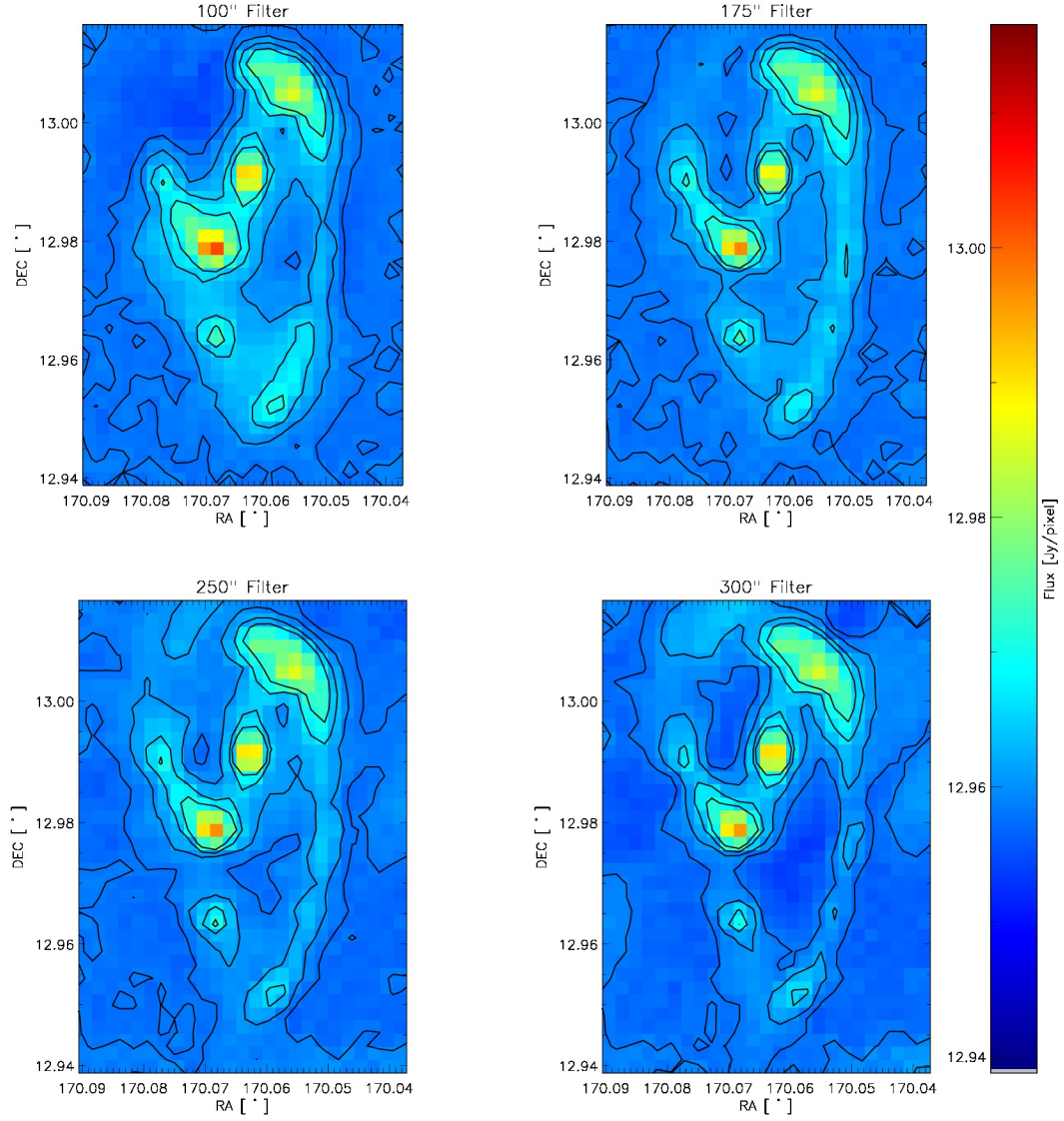
Figure 2.3: Four 850μm maps of NGC3627 using varying high-pass filter sizes. The contours shown are for 0.0, 0.002, 0.005, and 0.008 Jy/pixel for each image.
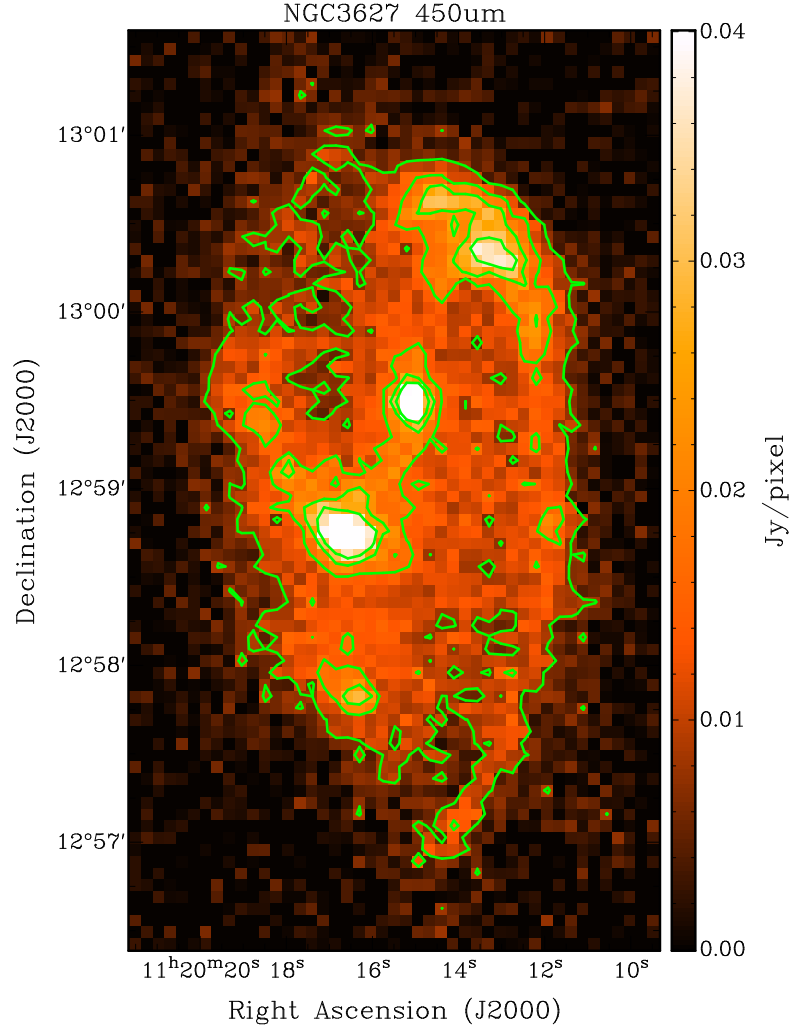
NGC3627 450um

Figure 2.4: 450μm observation produced at the end of the image production with 20%, 40%, 60%, and 80% contours.

Table 2.1.   Properties of NGC3627 SCUBA-2 Observations

Observation	Beam Properties				RMS
	α	θ_α	β	θ_β	$[mJy\ /\ Pixel]$
450μm	0.854 ± 0.002	$7.48'' \pm 0.03''$	0.146 ± 0.003	$23.1'' \pm 0.2''$	3.42
850μm	0.9624 ± 0.0002	$12.8'' \pm 0.004''$	0.0376 ± 0.0002	$44.5'' \pm 0.09''$	0.476

28

Figure 2.5: 850μm observation produced at the end of the image production with 20%, 40%, 60%, and 80% contours.

2.2.1 Beam Shape of the 450μm and 850μm Data

The Uranus calibration images were used to determine the shape of the beam for the 450μm and 850μm observations. The beam shape of both the 450μm and 850μm maps deviates from a single gaussian due to the second maximum of t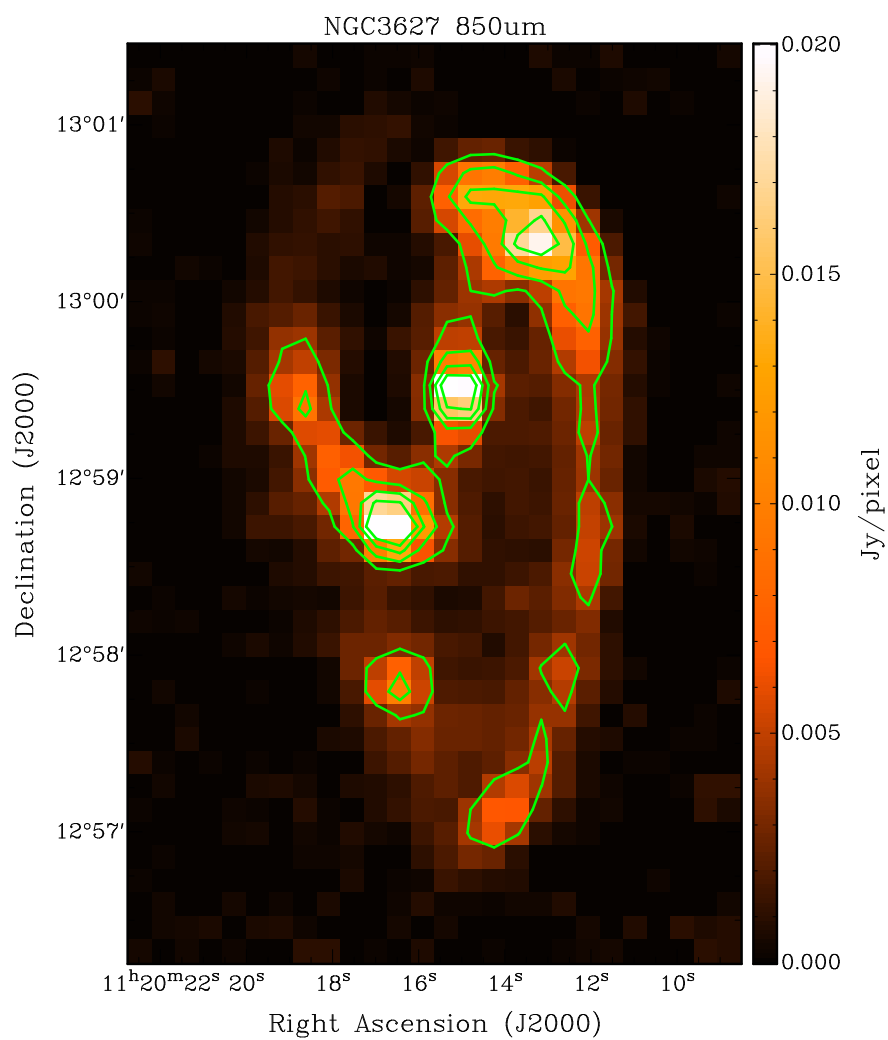he airy diffraction pattern in the response function of the telescope and minor imperfections in the mirror of the JCMT due to boundaries of the panels (Dempsey et al., 2013). This abnormality is best represented by a sum of two gaussians whose amplitude totals to unity (Dempsey et al., 2013). The average beam resolution for the 450μm and 850μm are reported in Table 2.1 and match the values within uncertainty found in Dempsey et al. (2013). The calibration images, fitted beams, and the residual of the fits can be seen in Figure 2.6. The contribution of the error beam in the 850μm emission is negligible, and allows the beam to be approximated by a single gaussian. However, the contribution of the error beam in the 450μm images was large enough to require special treatment in order to properly match the beams for analysis.

2.3 Ancillary Data

The scientific goals of this thesis required data outside the capabilities of SCUBA-2. For instance, accurately determining the dust mass involved fitting the spectral energy distribution (SED) for NGC3627. To successfully fit an SED, we needed shorter wavelength data to fully probe the cold component of this galaxy. We used data ranging from 100μm to 500μm from the KINGFISH survey (Kennicutt et al., 2011) to gain a large enough wavelength range for fitting the cold component. Secondly, the bandpass of the 850μm emission

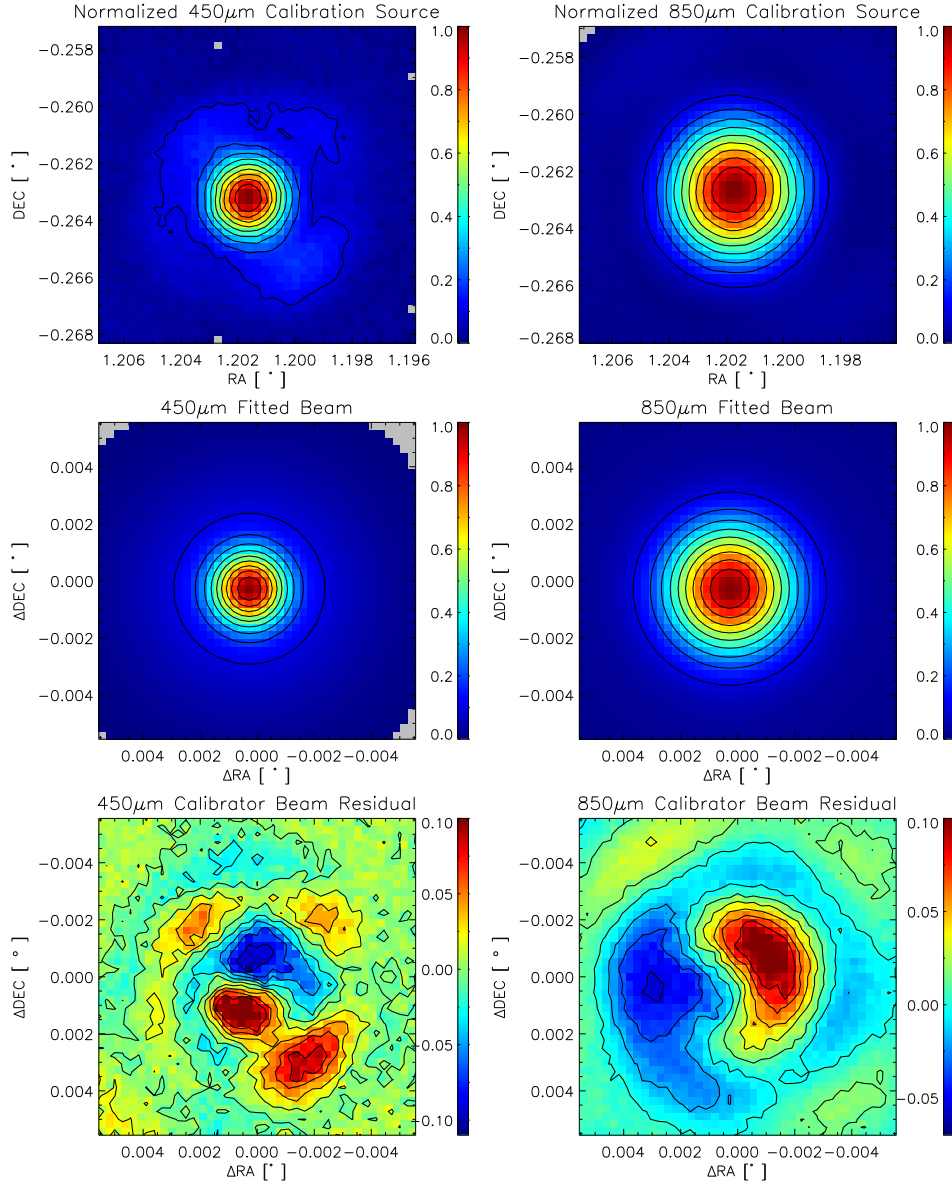Figure 2.6: The top row shows the Uranus images taken on January, 8th 2012 for the 450μm on the left and the 850μm on the right. The middle row shows the fitted beams for the 450μm on the right and 850μm on the left using the double gaussian beam shape. The bottom row shows the difference between the original image and the fitted beam. The contours in the image are from 10% to 90% in intervals of 10%.

contains the CO J=3-2 transmission line. In order to get a valid measurement of the dust mass, this contribution had to be removed. We used emission data from the NGLS using the HARP instrument on the JCMT (Wilson et al., 2012) to fulfill this role. When a dust mass was obtained, we used CO J=1-0 from the Nobeyama 45-m telescope (Kuno et al., 2007), CO J=2-1 from HERACLES (Leroy et al., 2009), and HI observations from THINGS (Walter et al., 2008) to determine a reasonable molecular hydrogen mass to calculate a dust-to-gas ratio.

2.3.1 Key Insights on Nearby Galaxies: a Far-Infrared Survey with Herschel (KINGFISH)

The Key Insights on Nearby Galaxies: a Far-Infrared Survey with Herschel (KINGSFISH) was designed to be a follow up to the Spitzer Infrared Nearby Galaxies Survey (SINGS) (Kennicutt et al., 2003) with observations of the warm and cold component of dust emission using the increased resolution from Herschel (Kennicutt et al., 2011). The main science goals of the KINGFISH survey were to better understand the star formation processes that were shielded by dust, resolved studies of heating and cooling of the interstellar medium (ISM), and to build an inventory of how cold dust emission relates to other dust components in the ISM (Kennicutt et al., 2011). The survey consisted of studying 61 nearby galaxies (d<30Mpc) that cover a range of environments. Each target was observed at 70μm, 100μm, 160μm, 250μm, 350μm, and 500μm. Our analyis focuses on fitting the cold component of NGC3627's SED, so we omitted the 70μm emission from the fitting, and pro-

Table 2.2.   Properties of NGC3627 KINGFISH Observations

Observation	Beam Properties θ_{beam}	RMS [mJy/Pixel]	Percentage of Emission Removed
100μm	$6.8''$	2.24	11%
160μm	$11.6''$	3.95	17%
250μm	$18.0''$	2.47	20%
350μm	$24.9''$	1.08	21%
500μm	$36.0''$	0.387	28%

cessed the data through MAKEMAP as described in § 2.4. The rms and beam size after the large scale structure has been removed can be seen in Table 2.2, while the preconvolved maps are shown in Figures 2.7 to 2.11.

2.3.2 Nearby Galaxies Legacy Survey (NGLS)

The Nearby Galaxies Legacy Survey is an HI-selected set of 155 galaxies contained in the annulus of $2Mpc \leq r \leq 25Mpc$ observed using the instrumentation on the JCMT (Wilson et al., 2012). The NGLS consists of data observed in several wavelengths that include the 450μm and 850μm data used for this thesis. As mentioned previously, the bandpass for SCUBA-2's 850μm emission contains the CO J=3-2 line which is contained in the NGLS data set. We used the zeroth moment CO J=3-2 maps from the NGLS to determine the percentage of CO J=3-2 emission present in the 850μm band as well as removing it for an accurate SED analysis. The rms and resolution of the CO J=3-2 emission are shown in Table 2.3, and the scan prior to convolution is shown in Figure 2.12.
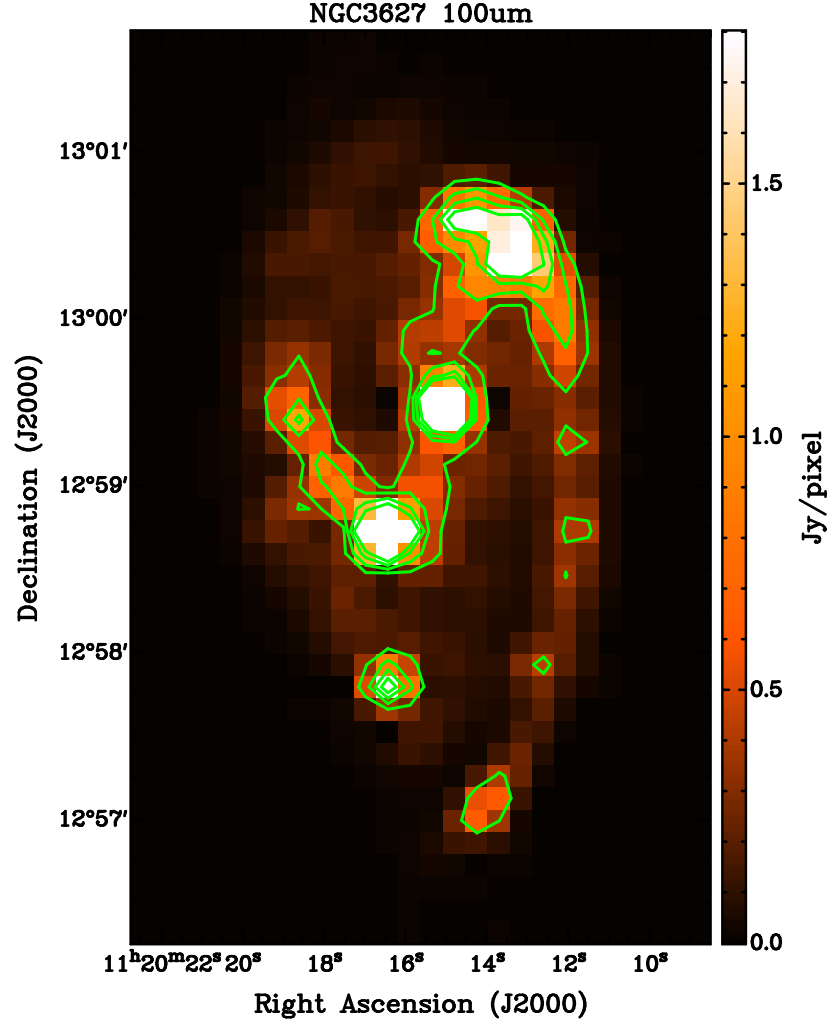
Figure 2.7: Image after the MAKEMAP filtering of 100μm observations with 20%, 40%, 60%, and 80% contours.

Table 2.3.   Properties of NGC3627 NGLS Observations

Observation	Beam Properties θ_{beam}	RMS $[mJy/Pixel]$	Percentage of Emission Removed
CO J=3-2	14.5″	1.28e-2	29.8%

Figure 2.8: Image after the MAKEMAP filtering of $160\mu m$ observations with 20%, 40%, 60%, and 80% contours.

Figure 2.9: Image after the MAKEMAP filtering of 250μm observations with 20%, 40%, 60%, and 80% contours.

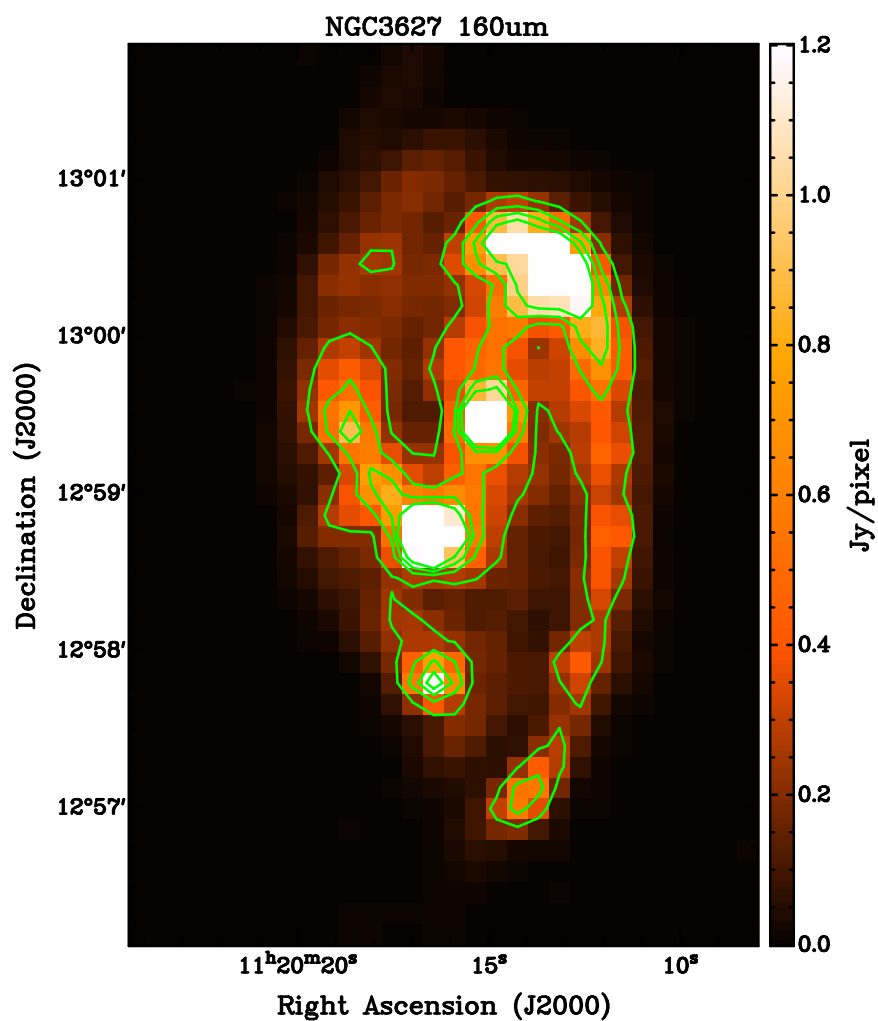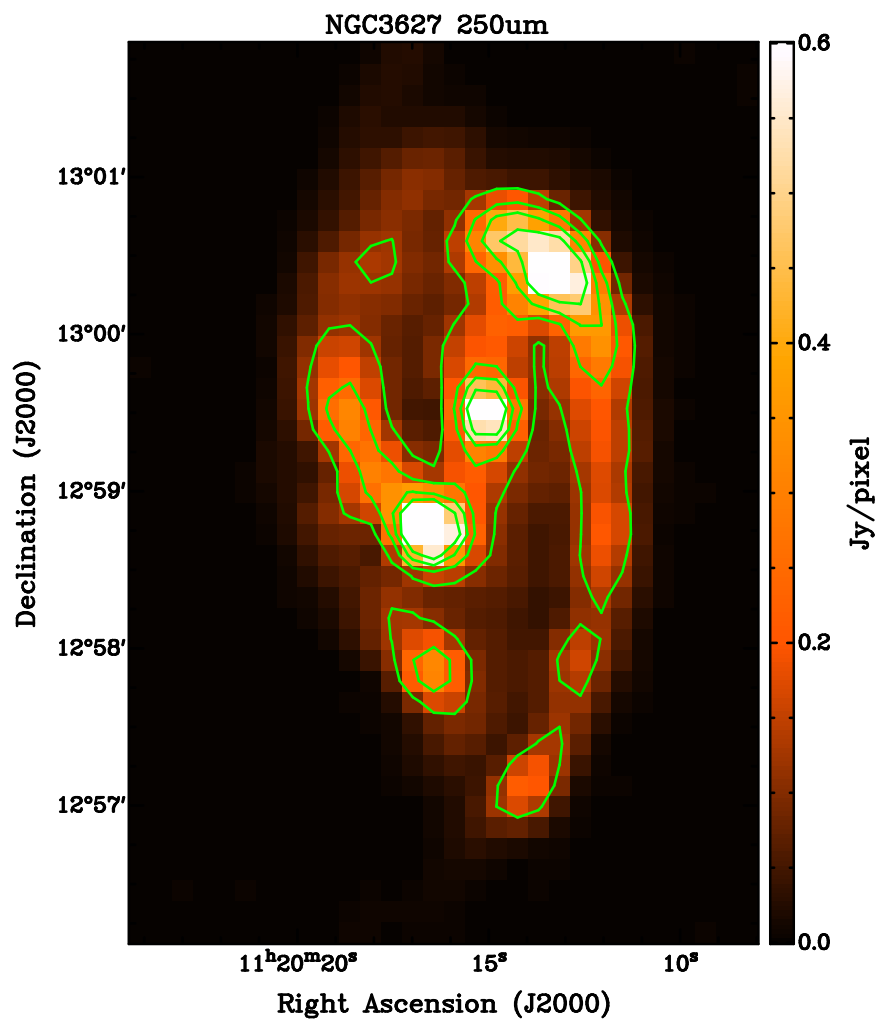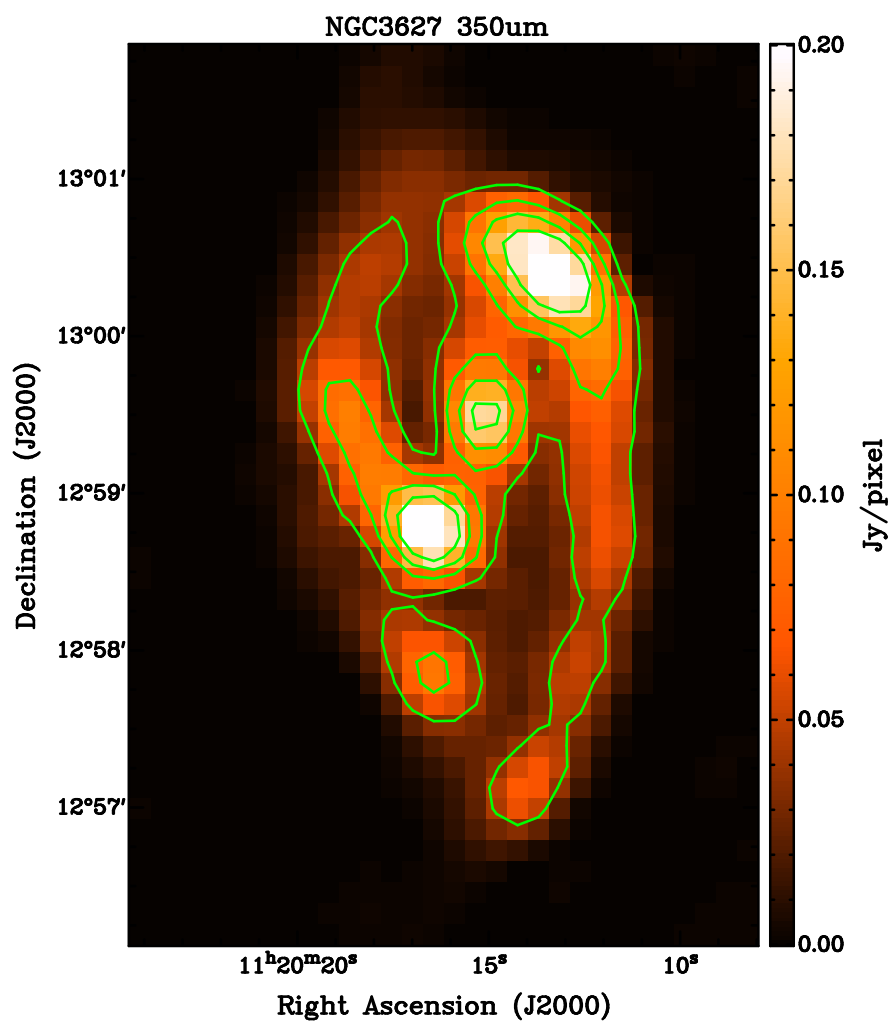Figure 2.10: Image after the MAKEMAP filtering of the 350μm observations with 20%, 40%, 60%, and 80% contours.
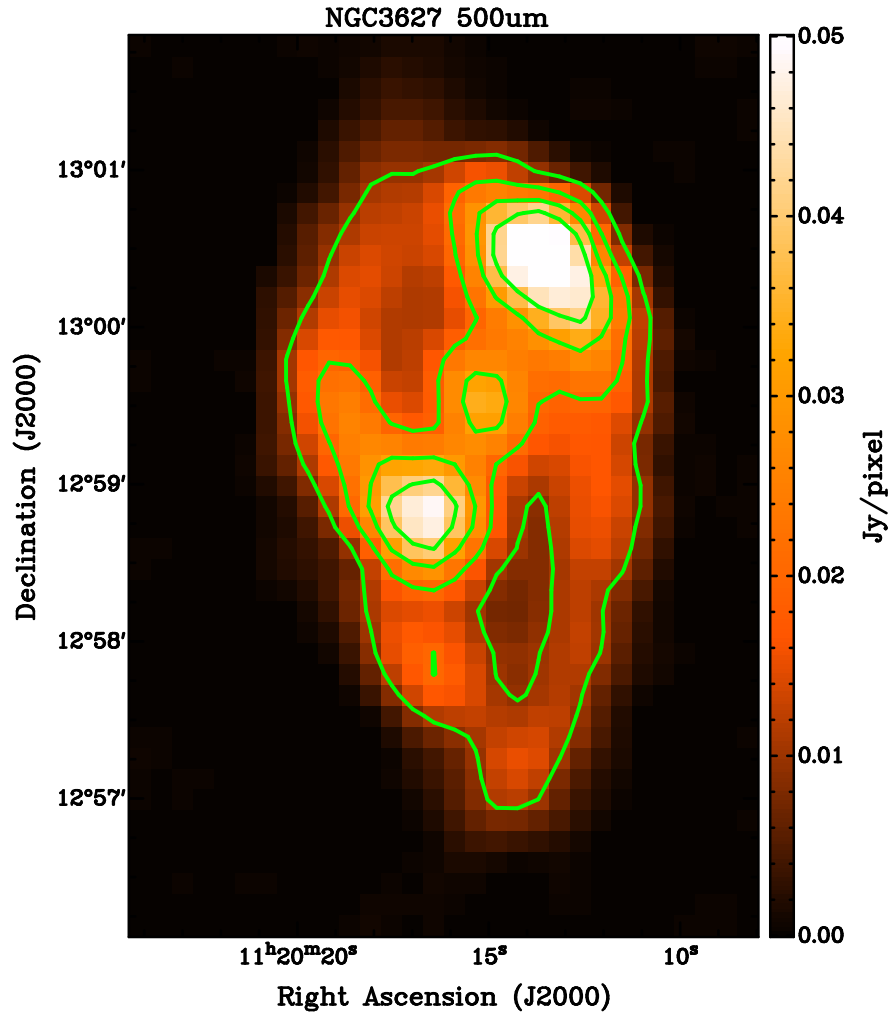
Figure 2.11: Image after the MAKEMAP filtering of the 500μm observations with 20%, 40%, 60%, and 80% contours.
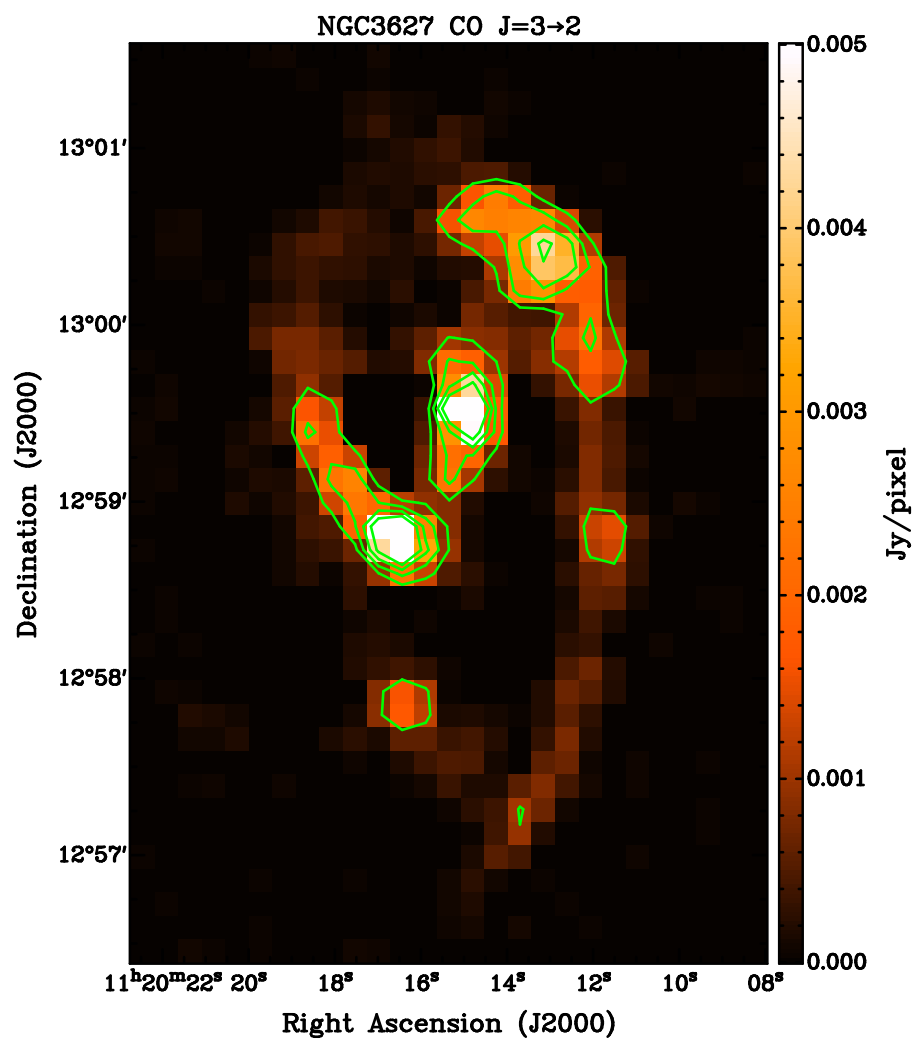
Figure 2.12: Residual of the MAKEMAP filtering of CO J=3-2 observations used to subtract line contamination from 850μm SCUBA-2 map with 20%, 40%, 60%, and 80% contours.

Table 2.4.   Properties of NGC3627 Nobeyama 45-m Observations

Observation	Beam Properties θ_{beam}	RMS $[K\ km/s]$	Percentage of Emission Removed
CO J=1-0	15.0″	0.681	20%

2.3.3 Nobeyama 45-m

Determining a dust-to-gas ratio requires a molecular tracer to estimate the amount of molecular hydrogen present. The most frequently used tracer is CO J=1-0 due to its abundance in the ISM. The CO J=1-0 we used was taken from the Nobeyama 45-m CO Atlas of Nearby Spiral Galaxies observed to better understand the role of bars relating to molecular gas (Kuno et al., 2007). The Nobeyama 45-m CO Atlas consists of galaxies with morphologies ranging from Sa to Scd, located less than 25Mpc from the Milky Way, inclination values less a than 79°, 100μm flux greater than 10Jy, and spiral structure that has not be compromised through interactions. Any galaxies that met these criteria were then observed with the Nobeyama 45-m telescope (Kuno et al., 2007). The beam sizes and rms of the filtered CO J=1-0 map are displayed in Table 2.4 and the final image product can be seen in Figure 2.13.

2.3.4 Hetrodyne Reciever Array CO-Line Extragalactic Survey (HER-ACLES)

The CO J=2-1 line was used to determine a CO $2-1/1-0$ line ratio which can be used to trace a gradient in α_{CO} and hint towards regions of

Figure 2.13: Residual of the MAKEMAP filtering of CO J=1-0 observations with 20%, 40%, 60%, and 80% contours.

Table 2.5.   Properties of NGC3627 HERACLES Observations

Observation	Beam Properties θ_{beam}	RMS $[K\ km/s]$	Percentage of Emission Removed
CO J=2-1	13.0″	0.305	7%

high star-formation (Reuter et al., 1996). We used the CO J=1-0 data from the Nobeyama 45-m telescope (§ 2.3.3), and CO J=2-1 from the Hetrodyne Reciever Array CO-Line Extragalactic Survey (HERACLES) using the IRAM 30-m telescope. The main goal of HERACLES was to quantify the relationship between atomic and molecular gas and star formation using a large sample of galaxies (Leroy et al., 2009). The sample of galaxies chosen were targets contained in THINGS that were within the observing limits of the IRAM 30-m telescope. The final image can be seen in Figure 2.14 and the image properties can be seen in Table 2.5.

2.3.5 The HI Nearby Galaxy Survey (THINGS)

To determine the gas to dust ratio we had to determine the total amount of gas present which includes both atomic and molecular hydrogen. We approximated the amount of molecular hydrogen by using CO J=1-0, and measured the amount of atomic hydrogen (HI) present. The source of our atomic hydrogen came from The HI Nearby Galaxy Survey (THINGS) designed to observe HI emission in nearby galaxies with the extreme spatial resolution of the Very Large Array (VLA). Targets in THINGS included many of the SINGS targets
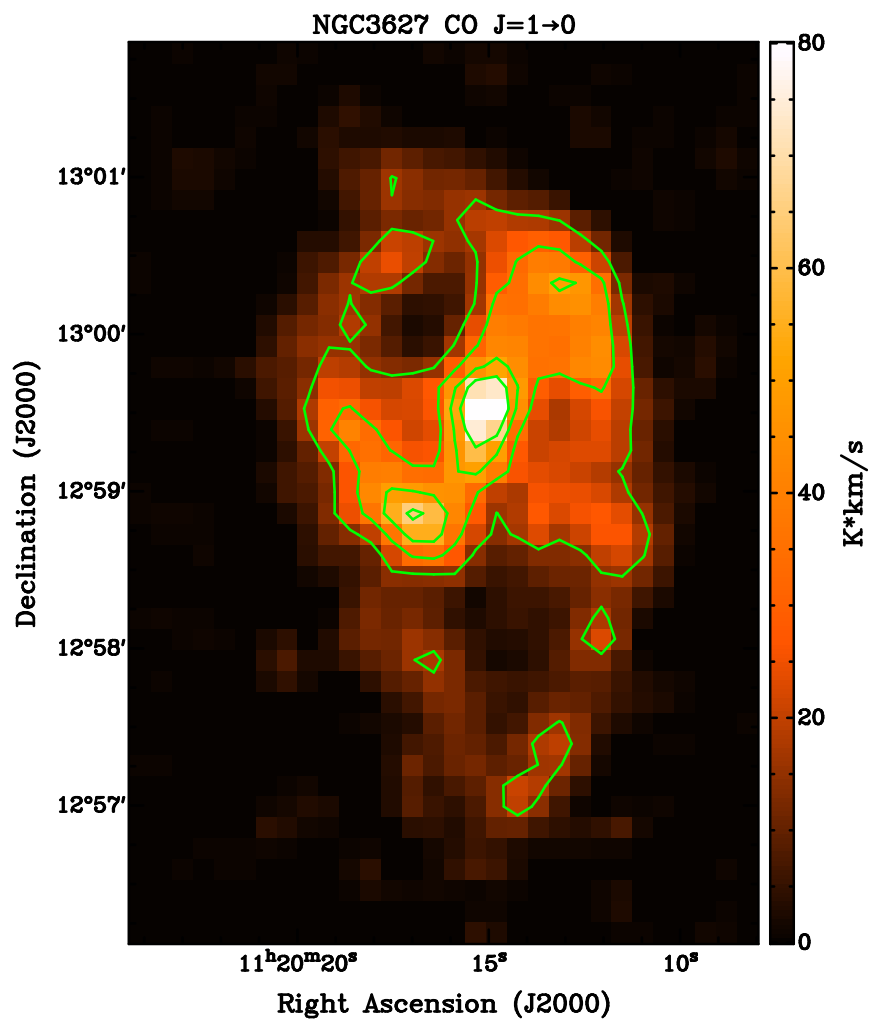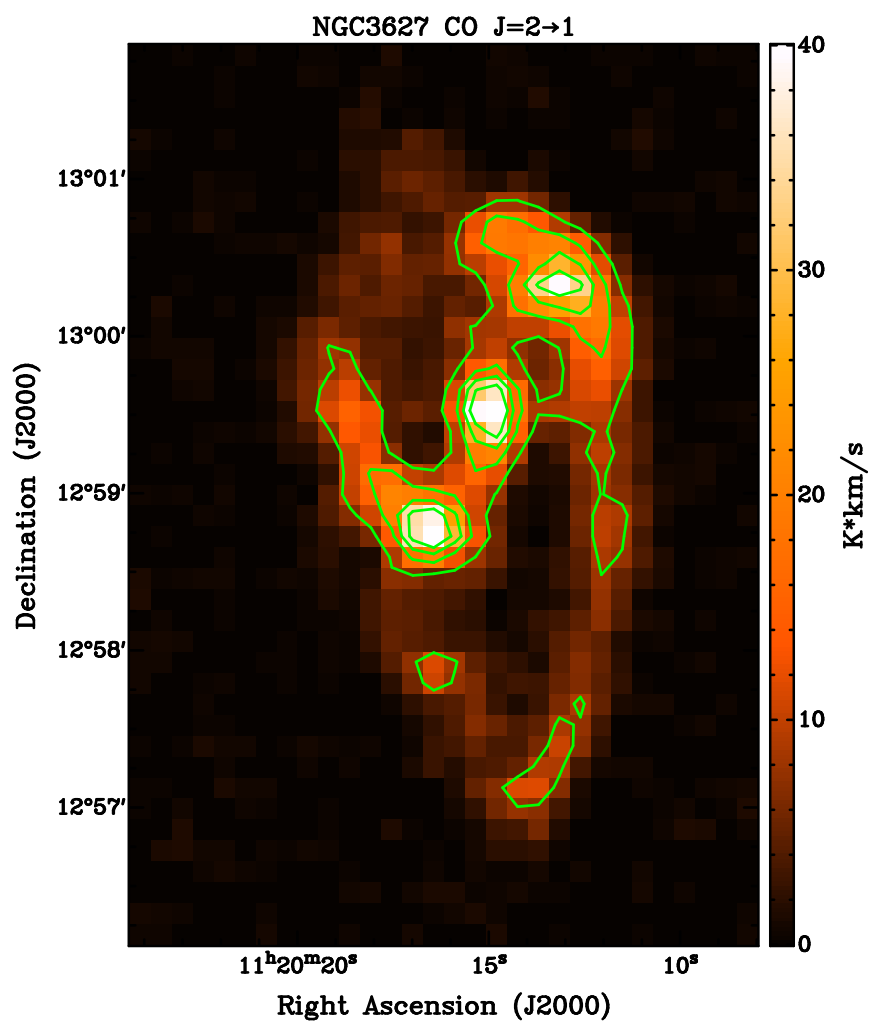
Figure 2.14: Residual of the MAKEMAP filtering of CO J=2-1 observations with 20%, 40%, 60%, and 80% contours.

Table 2.6.   Properties of NGC3627 THINGS Observations

Observation	Beam Properties			RMS	Percentage of Emission Removed
	θ_{maj}	θ_{min}	θ_{PA}	$[M_\odot/pc^2]$	
HI	10.6″	8.85″	-48.0°	0.760	>99%

with the exception of known HI poor sources (E/S0 type galaxies), dynamically complex systems (edge-on spirals), and large extended galaxies found in the Local Group (Walter et al., 2008). The resolution and rms of the filtered image are shown in Table 2.6. The final data product is shown in Figure 2.15 which has been converted to $M_\odot$ pc^{-2} using

$$M_{HI}\,[M_\odot] = 2.36 \times 10^5 D^2 \times \sum_i S_i \Delta v \qquad (2.2)$$

Walter et al. (2008) and then dividing by the pixel area in pc^2 where D is the distance, and $\sum_i S_i \Delta$v is the first moment of the flux.

2.4 Data Preparation for Analysis

Initially the data do not agree on several levels. The differences consist of the presence of the large scale/extended structure and different resolutions including the beam shape of the 450μm. We have taken several steps to correct these disagreements and maximize the compatibility of the data. In order to account for the varying beam resolutions, we use a gaussian convolution to increase the resolution of our maps to the largest beam size in our dataset, σ_{max}=36″. An appropriate convolution beam width is determined by
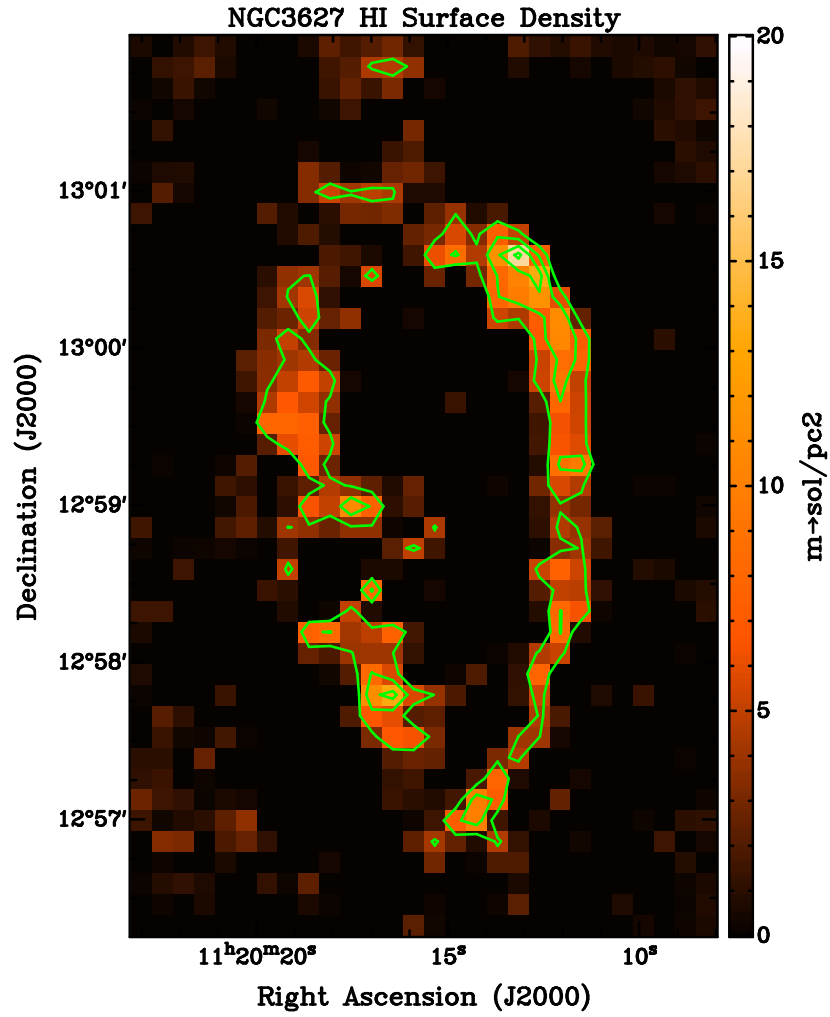
Figure 2.15: Residual of the MAKEMAP filtering of HI observations with 20%, 40%, 60%, and 80% contours.

$$\sigma_{desire} = \sqrt{\sigma_{max}^2 - \sigma_{given}^2} \qquad (2.3)$$

such that σ_{desire} is the desired beam width, σ_{max} is the beam size we are convolving to, and σ_{given} is the beam size we are convolving from.

However, this only works when the beams are well approximated by a gaussian which is not the case for the 450μm beam. The steps taken to match the resolution of the 450μm beam with the rest of the data set are given in §2.4.1. Removing any large scale structure from our ancillary data is implemented using a feature built into MAKEMAP that allows us to add fake sources into the data during production. The fake source implementation allows us to remove the same amount of large scale structure from our ancillary data as was removed from the SCUBA-2 data. The steps taken to prepare the ancillary data are described in §2.4.2.

2.4.1 Accounting for the 450μm Error Beam

Taking the 450μm error beam into consideration is different than a normal beam convolution in the sense that we are not convolving the higher resolution map to the lowest resolution. Instead we are adding in an error beam similar to the error beam found in the 450μm observations. We have to take these steps because convolving a double gaussian beam with a single gaussian kernel will not sufficiently remove the error component of our beam resulting in a poor approximation to the wings of our beam shape.

In order to accommodate the 450μm map's error beam, we used a method employed by another SCUBA-2 survey, the Gould Belt Survey team. This method used the distributive nature of the Fourier transform to create similar error components in the beams we were convolving to and from. Carrying out this convolution involved breaking the 450μm beam into its two components, X_α and X_β to represent the main beam and error beam. The values of the main beam amplitude, X_α, and error beam amplitude, X_β, will sum to one so the height of the total beam is normalized to one. The poorest resolution beam, X_{max}, is convolved with the two components X_α and X_β and the resulting beams are added together. This process produces an equivalent two component beam as the 450μm beam convolved with X_{max}. The relationship can be expressed as

$$
\begin{aligned}
X_{max} * X_\alpha + X_{max} * X_\beta &= (X_\alpha + X_\beta) * X_{max} \\
&= X_{450\mu m} * X_{max}
\end{aligned}
\tag{2.4}
$$

Where X_{max} is the poorest resolution beam, X_α and X_β are the main and error beam of the 450μm observations, and $X_{450\mu m}$ is the double gaussian beam shape of the 450μm observations.

2.4.2 Extended Structure Removal via MAKEMAP

Due to the combination of methods used in MAKEMAP, large scale/extended structure is removed from the final SCUBA-2 images. However, in all of our ancillary data the large scale emission was present in the initial maps. The removal of the extended features from our support data was carried out by

passing the data through MAKEMAP using a special function called fakemap. Implementing fakemap allows us to pass an image though processing and have it added into the image being processed. We use the 850μm map as our base image for the filtering process and add the ancillary data to the image. The output image then consists of the sum of the ancillary data and the 850μm map. The ancillary data were then isolated by subtracting the 850μm image from the fakemap image.

Preparing the data to be implemented consisted of either converting the images from their native units into pW using the 850μm flux calibration factor and scaling down to match the observed signal or by just applying a scaling factor. Which method is used is based on the desired units of the final map, and can be separated by what purpose the data had in our analysis.

The data used in the SED fitting (KINGFISH and NGLS) were scaled to pW so they could have a similar reduction and calibration process as the SCUBA-2 maps. The KINGFISH data is regridded to a $2''$ by $2''$ pixel size and has the appropriate calibration factor from Dempsey et al. (2013) applied to convert from either MJy/sr to pW in the case of the 250μm, 350μm, and 500μm or from Jy/pixel to pW for the 100μm and 160μm. Converting the CO J=3-2 requires the final product to be in the same units as the 850μm observations in order to properly remove its molecular gas contribution. Converting from K km/s to mJy/beam involved applying a scaling constant of 0.70 [mJy/beam][K km/s]$^{-1}$ (Drabek et al., 2012) prior to applying the 850μm flux calibration factor to convert to pW. After the data has been converted to pW, the image used as a fakemap is then scaled down to the same order of magnitude as the

base image using a scaling factor specified prior to the map production. After the fakemap image has been processed and the 850μm map subtracted, the maps are scaled back up using the scaling factor used to scale them down and calibrated using the same flux calibration factors as the 850μm map and scaled to an $8''$ by $8''$ grid. The amount of extended flux lost in the KINGFISH and NGLS is shown in Tables 2.2 and 2.3. This process is shown in Figure 2.16 from the original Herschel 100μm map, to the final image used in SED fitting convolved to the 500μm beam resolution, $36.0''$.

The rest of the ancillary data is used in calculating a dust to gas ratio, and follows nearly the same process as the SED data filtering. The major difference is the CO J=1-0, CO J=2-1 and HI maps need to remain in their original units of K km/s and $M_\odot/pc^2$. This necessity simplified the process by only requiring a scaling factor of 0.001 to be applied to the original maps. After the data is scaled, it is filtered using the fakesource option in MAKEMAP with the 850μm observation as the base image. The atomic and molecular gas maps were then isolated in the same fashion as the KINGFISH and NGLS, however they were rescaled back to their original values and fit to an $8''$ by $8''$ grid then finally convolved to a $36.0''$ resolution. The process is shown in Figure 2.17. The amount of emission lost is shown in tables 2.4, 2.5, and 2.6.
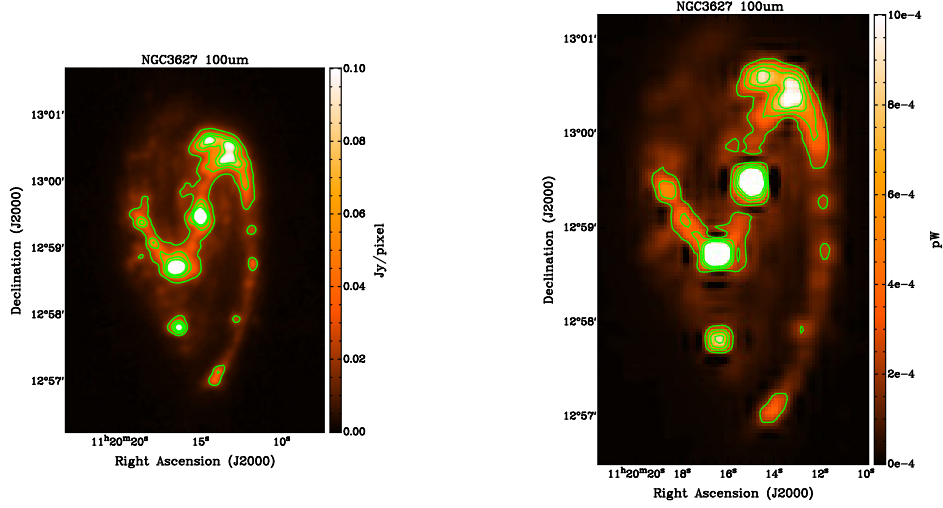
(a) Herschel 100μm image of NGC3627.

(b) Herschel 100μm image converted to pW and rescaled to a $2''$ by $2''$ pixel grid.
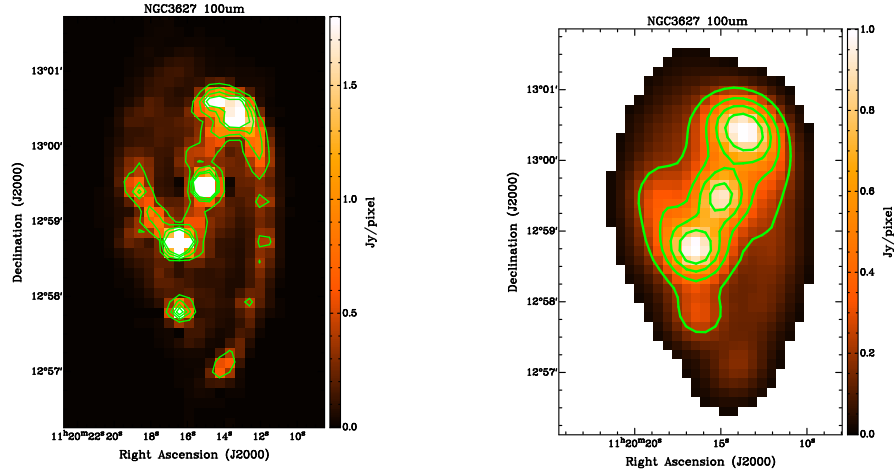
(c) 100μm map of NGC3627 after large scale structure has been removed and rescaled to an $8''$ by $8''$ grid.

(d) 100μm map with extended structure removed and convolved to final resolution of $36.0''$ with a 5σ cut applied.

Figure 2.16: The 100μm image from the beginning of processing to the end of processing. All of the contours shown are 20%, 40%, 60%, and 80%.
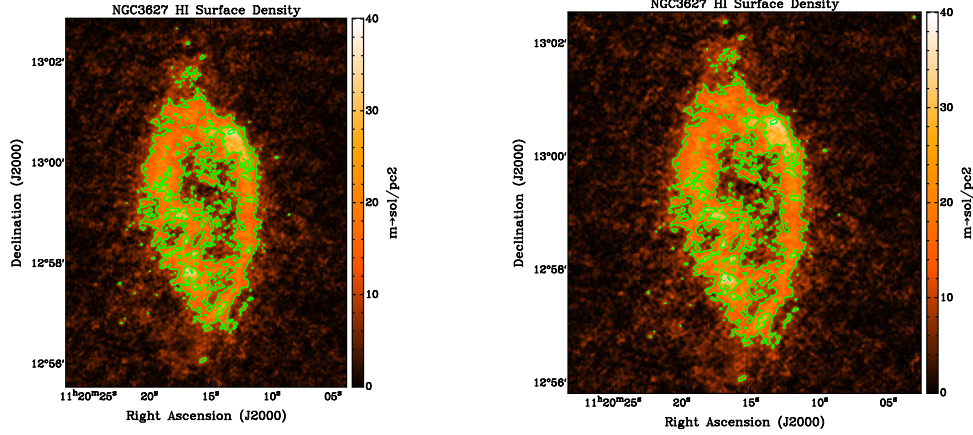
(a) HI surface density map of NGC3627.

(b) HI surface density map rescaled to a $2''$ by $2''$ pixel grid.
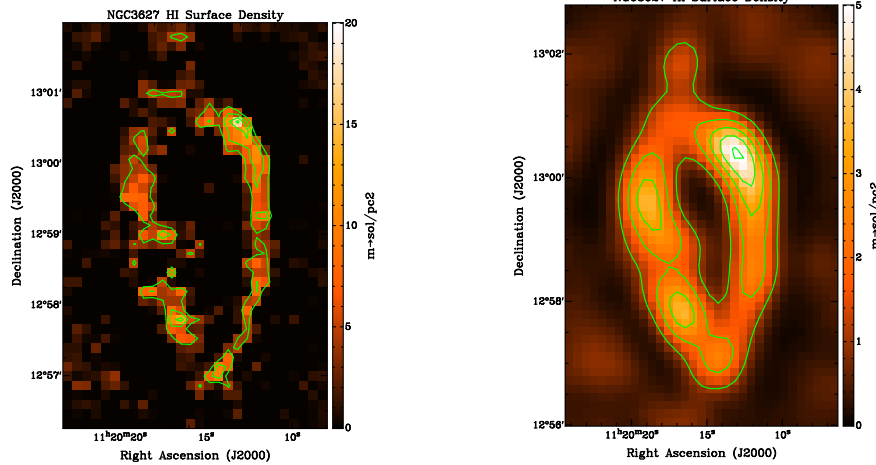
(c) HI surface density map of NGC3627 after large scale structure has been removed and rescaled to an $8''$ by $8''$ grid.

(d) HI surface density map with extended structure removed and convolved to final resolution of $36.0''$.

Figure 2.17: The HI surface density maps from the beginning of processing to the end of processing. The contours in the top row are 30%, 60% and 90%, and the contours in the bottom row are 20%, 40%, 60%, and 80%.

Chapter 3

Spectral Energy Distribution Analysis

3.1 SED Fitting Method

In order to determine a dust mass, we use the IDL package MPFIT (Markwardt, 2009) to fit equation

$$S_\nu(T) = \frac{M\,\kappa_{\nu,0}}{D^2}\left(\frac{\nu}{\nu_0}\right)^{\beta+3} B_\nu(T) \tag{3.1}$$

for the temperature, T, mass, M, and the emissivity index, β while the opacity, $\kappa_{\nu,0}$, distance, D, and reference wavelength, ν_0 are held fixed. The routine MPFIT utilizes the Levenberg-Marquardt algorithm. This algorithm uses a combination of two minimization techniques (the steepest descent method and the Newton-Raphson Method) to determine the parameter combination that corresponds to a minimum in the χ^2 space while maximizing the efficiency of the step sizes in each iteration (Burden & Faires, 2001). The algorithm begins by implementing the steepest descent method. The way this technique works is it will follow the direction opposite to the largest gradient in order to traverse the χ^2 space to locate a minimum. As the set of solutions approaches

Table 3.1.   Systematic Calibration Uncertainties for SCUBA-2 and
KINGFISH Observations

Observation	Scaling Factor
100μm	3%
160μm	5%
250μm	7%
350μm	7%
450μm	12%
500μm	7%
850μm	8%

a minimum, it will switch to the Newton-Raphson method to locate the best set of parameters by finding where the derivative at that point is closest to zero (Gavin, 2013).

In order for MPFIT to provide the most accurate fit, we establish a reasonable error for each of our data points, and determine a realistic set of starting points for the fitting. The variance for our SCUBA-2 data is determined using

$$\sigma^2 = \sigma^2_{obs} + \sigma^2_{rms,sky} + \sigma^2_{calib} \tag{3.2}$$

such that σ_{obs} is the noise determined by MAKEMAP, $\sigma_{rms,sky}$ is the RMS of the sky, and σ_{calib} is the product of calibration uncertainty and observed flux for each observed wavelength. The systemic calibration scaling factors are shown in Table 3.1.

The variances for the KINGFISH data are determined in a similar fashion using

$$\sigma^2 = \sigma^2_{rms,sky} + \sigma^2_{calib}. \tag{3.3}$$

The observation error is excluded since the reported variance in the filtered images are reflective of the fake source image used and not of the KINGFISH data set.

The nature of the Levinberg-Marquardt method leaves the solution vulnerable to converge at a local minimum rather than converging at the global minimum. This is remedied by selecting reasonable initial conditions. The initial conditions we used were a modified blackbody with a temperature of 20K, a dust emissivity index of 2, and a mass determined by

$$\begin{aligned}
M &= \frac{D^2 \, S_{250}}{\kappa_{\nu,0} \, B_{250}\left(T\right)} \left(\frac{\nu}{\nu_0}\right)^{-(\beta+3)} \\
&= 2.24 \times 10^5 \, S_{250} \; [M_\odot]
\end{aligned} \tag{3.4}$$

using the flux from the 250μm emission and our initial temperature and dust emissivity index values with a reference opacity of 0.2665 m^2 kg^{-1} at 300μm. When the best fit values have been calculated we use equation 3.4 to determine the dust mass associated with the 250μm emission instead of using the fitted peak mass in order to increase the signal to noise of our data and avoid any temperature dependences associated with emission further from the Rayleigh-Jeans tail of the SED. The error in the dust mass is then determined by taking the total derivative of the mass function with respect to each of the free variables.

3.2 Fitting the Spectral Energy Distribution

The fitting procedure was carried out in two different ways on a modified blackbody equation. One of the two methods is fitting an SED to each individual pixel in order to generate a set of parameter maps. The second method sums the flux of each of the selected regions shown in Figure 3.1 to maximize the signal to noise ratio in order to generate a more precise set of parameters. For both of the fitting methods the mass, M, and temperature, T, are set as free parameters, but the emissivity index, β, requires special treatment for each of the methods. The distance, D, has been set to 9.4 Mpc (Walter et al., 2008), and the reference opacity, $\kappa_{\nu,0}$, was tested using 0.2665 m^2 kg^{-1} (Li & Draine, 2001) and 1.0 m^2 kg^{-1} (Planck Collaboration et al., 2011).

3.2.1 Pixel SED Fits

In order to generate a parameter map of NGC3627, each individual pixel has its own SED determined from the available wavelengths described in the observations chapter. The fits are performed over 100μm, 160μm, 250μm, 350μm, 450μm or 500μm, and 850μm observations. Initially, we excluded the 500μm emission in order to increase the resolution of our final maps, but an over abundance of emission in the 450μm provided unreliable results, so we exchanged the 450μm emission with 500μm emission. The treatment of the dust emissivity index is performed by fixing it at $\beta = 1.8$ for the Planck opacity model where the opacity is $\kappa_{300\mu m,0} = 1.0$ m^2 kg^{-1} (Planck Collaboration et al., 2011) and $\beta = 2.0$ for the Li and Draine opacity model where the opacity is $\kappa_{300\mu m,0} = 0.2665$ m^2 kg^{-1} (Li & Draine, 2001). A third fit is performed
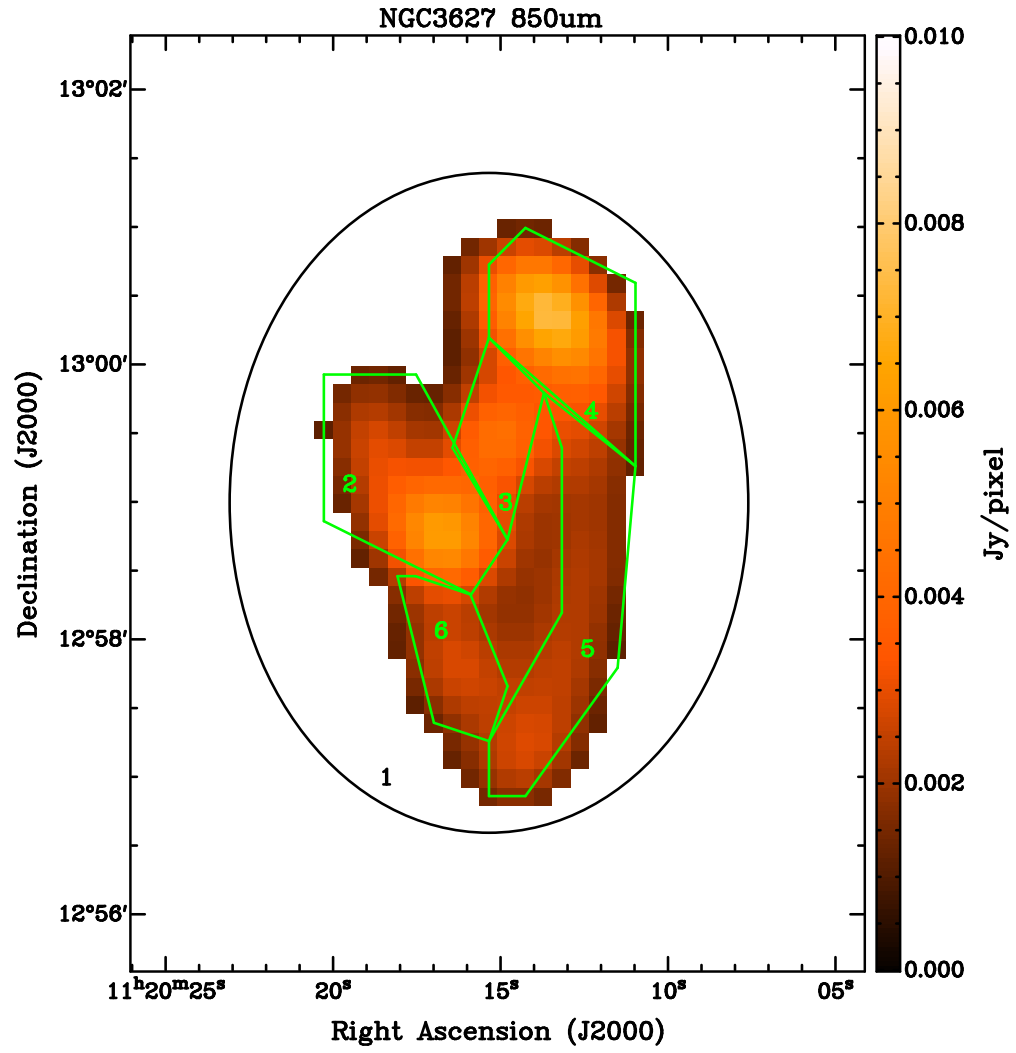
Figure 3.1: $850\mu m$ emission convolved to the $500\mu m$ beam size overlaid with the selected regions of NGC3627 labeled 1 through 6 such that region 1 includes the entire galaxy.

where the emissivity index is allowed to vary as a free parameter. While the emissivity index is allowed to vary, the opacity being used is the Planck model. Using either an opacity of 1.0 m^2 kg^{-1} or 0.2665 m^2 kg^{-1} will not effect the shape of the SED, only its normalizing value. In the case of our fits, it is the mass that acts as the normalizing value, so increasing or decreasing the opacity will yield the opposite effect in the mass. The inverse proportionality can be seen in equation 3.4.

The quality of the fit using the 450μm observations for the Li and Draine model of β=2 and $\kappa_{\nu,300}$=0.2665 is shown in Figure 3.2. The quality of the fit is determined by how well the expected flux from the SED fitting matches the observed flux. If the fits are able to recreate the observed emission, then all of the points will lie on the line $y = x$ shown in the plots as a black line. If the SED is underestimating the flux, the points will appear below the 1 to 1 line, and an over estimation from the SED will result in points above the line.

Using Figure 3.2, the fitting procedure is able to handle the 100μm, 250μm, and 850μm with some slight under estimation in the 160μm and over estimation in the 350μm. The most compelling piece of information in Figure 3.2 is the SED's inability to recreate the observed 450μm flux despite the care taken while accounting for the odd beam shape of the 450μm data. The discrepancy between the observed and fitted fluxes was not a result of a poor fit, but rather an intrinsic error in the 450μm observations. The over abundance of flux present in SCUBA-2 450μm data was determined to be an issue with the data itself rather than a signature of a physical process. Determining if the 450μm data was overestimating the flux was tested by extrapolating a
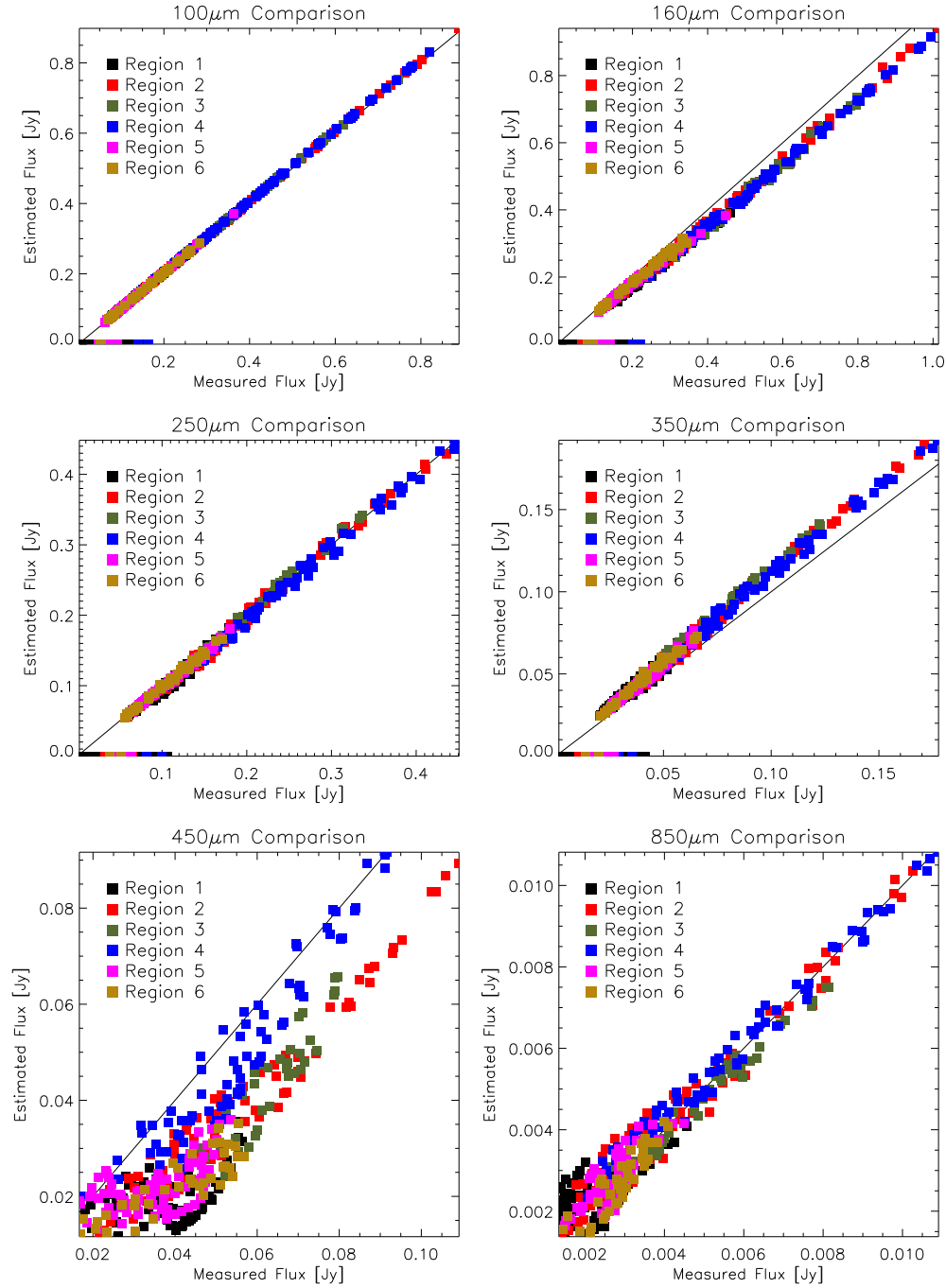
Figure 3.2: Quality of the SED fits to the Li and Draine model using the 450μm emission. The regions shown are the regions in figure 3.1.

Table 3.2.   Total Distance to 1 to 1 Line Using the 500μm Emission

Observation	Planck Model	Li and Draine Model	Variable Emissivity Index
100μm	0.000	0.01245	0.1277
160μm	15.55	8.979	2.159
250μm	5.808	3.071	0.4465
350μm	0.8045	0.3541	0.1161
500μm	0.08192	0.1147	0.1866
850μm	0.02825	0.05218	0.09528
Total	22.23	12.583	3.131

450μm flux using a linear fit between the filtered 350μm flux of 27.1 Jy and the filtered flux of the 500μm flux of 8.56 Jy. The flux expected from these two data points was 14.7 Jy, however our 450μ flux measured to be 20.6 Jy.

In order to avoid any errors in our final parameter maps, we substitute the 450μm emission with KINGFISH 500μm emission. The quality of fitted SEDs using the 500μm emission are shown in Figures 3.3, 3.4, and 3.5 for the Planck model, Li and Draine model and the emissivity as a free parameter respectively. To assign a numerical quantity to the quality of the fit the vertical distance was calculated for each point to the 1 to 1 line and then summed. The summed distances are shown in Table 3.2 and suggest the best fit comes from allowing the emissivity index to vary. The resulting parameter maps of the fits using the 500μm observations are shown in Figure 3.6. The numerical values from fitting each model are shown in Tables 3.3, 3.4, and 3.5 where each region corresponds to the regions labeled in Figure 3.1.
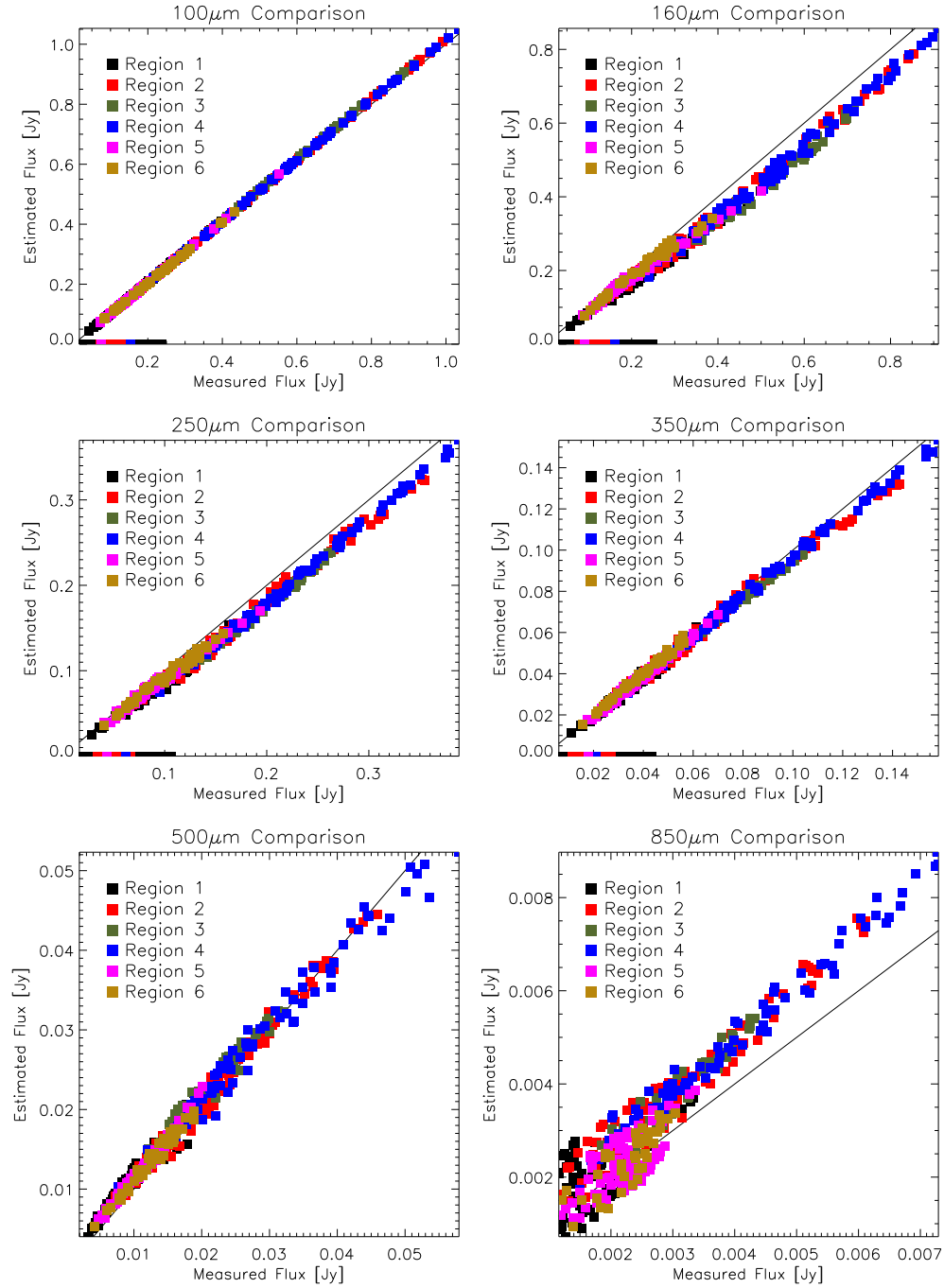
Figure 3.3: Quality of the SED fits using to the Planck model with the 500μm emission. The regions shown are the regions in figure 3.1.
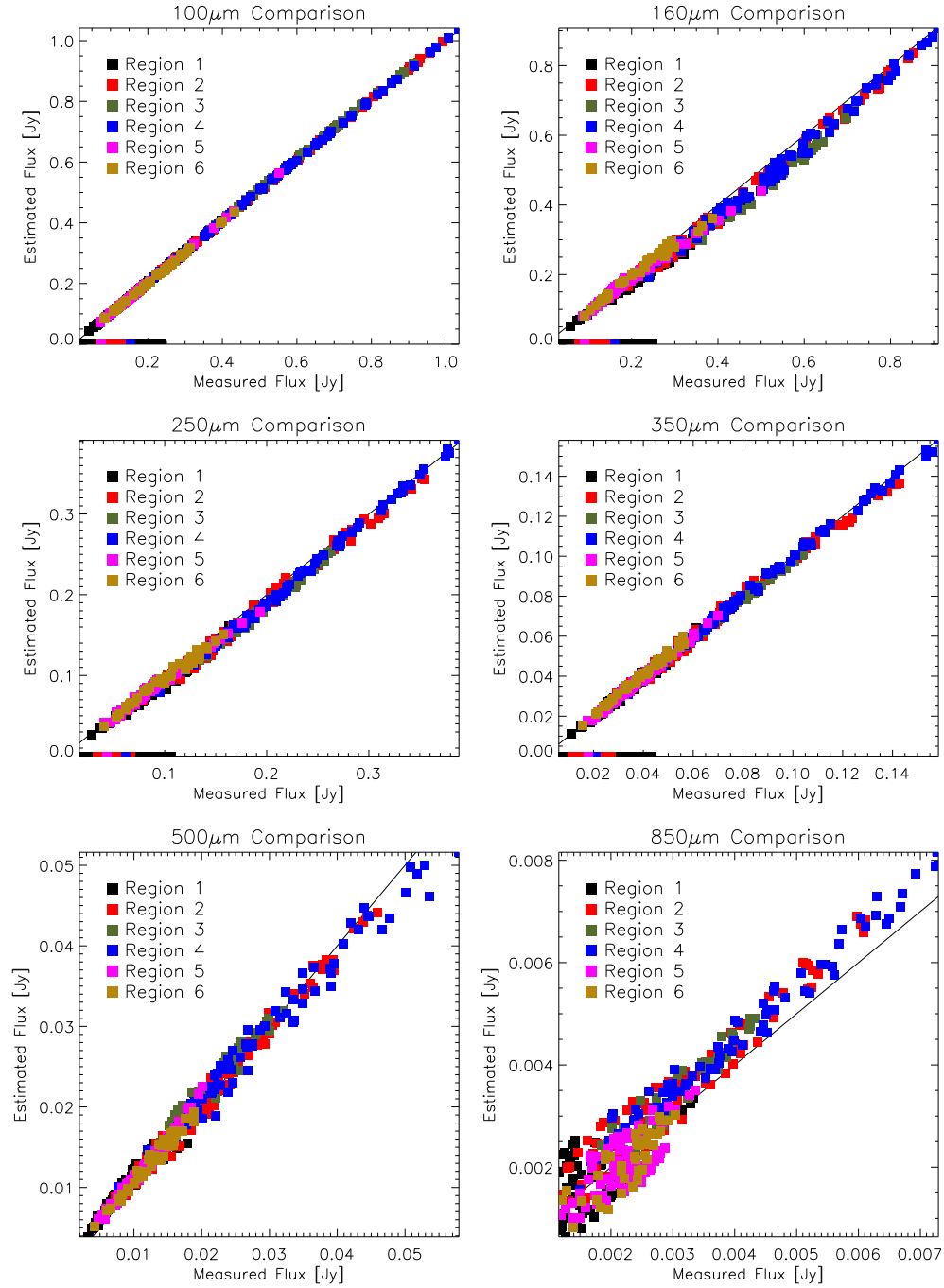
Figure 3.4: Quality of the SED fits using the Li and Draine model with the 500μm emission. The regions shown are the regions in figure 3.1.
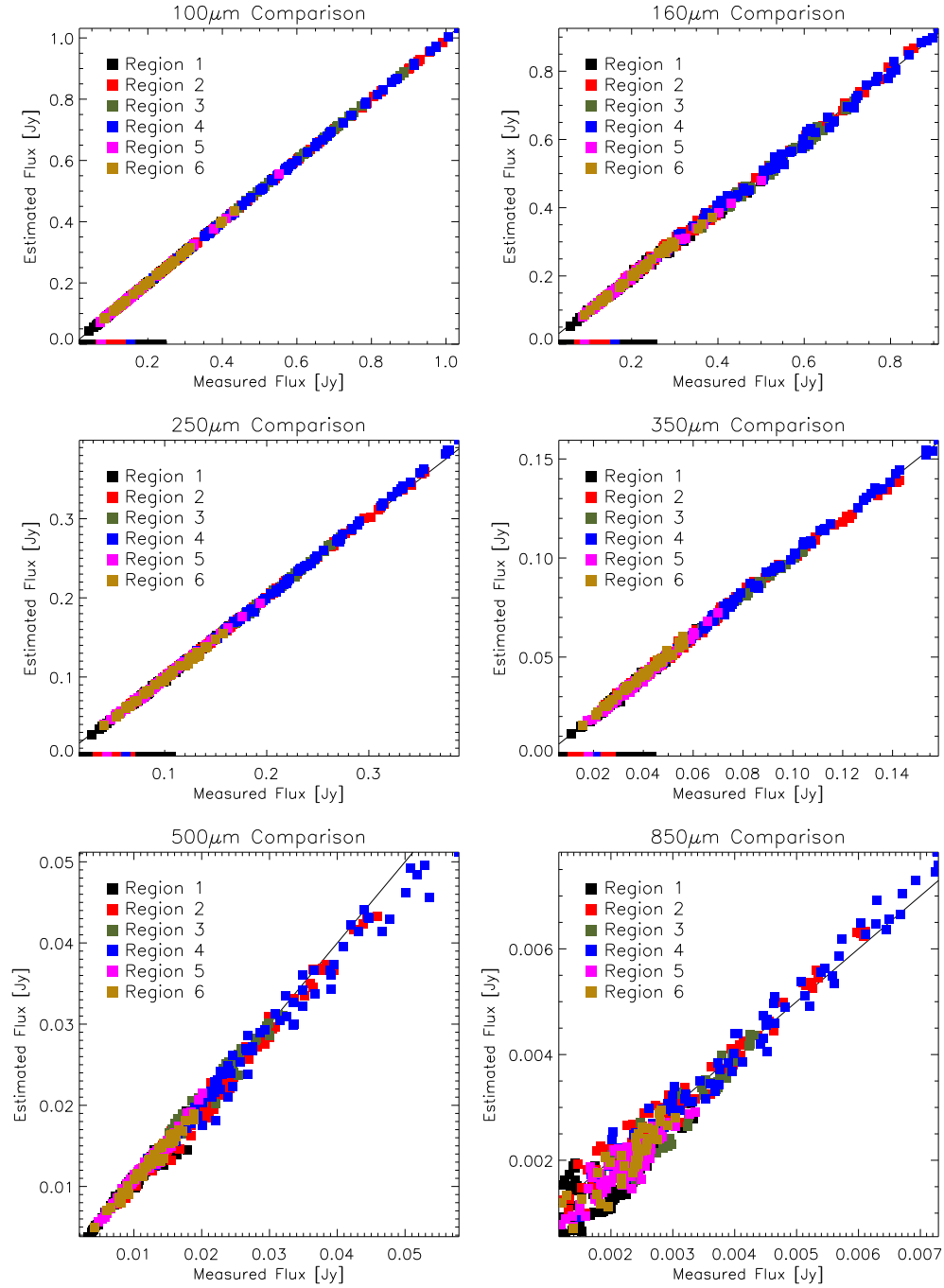
Figure 3.5: Quality of the SED fits with the emissivity index as a free paramter with the 500μm emission. The regions shown are the regions in figure 3.1.

Table 3.3.   Best Fit Parameters for Planck Model Using 500μm Emission for Pixel Fits

Region	Average β	Total Mass $[10^5 M_\odot]$	Average Surface Density $[M_\odot pc^{-2}]$	Average Temperature [K]
1	1.8	52 ± 23	0.10 ± 0.05	26 ± 2
2	1.8	13 ± 4	0.12 ± 0.04	27 ± 1
3	1.8	6 ± 1	0.12 ± 0.02	28.8 ± 0.6
4	1.8	16 ± 6	0.15 ± 0.05	26 ± 1
5	1.8	10 ± 2	0.08 ± 0.02	24 ± 1
6	1.8	4 ± 1	0.08 ± 0.02	25 ± 1

Table 3.4.   Best Fit Parameters for Li and Draine Model Using 500μm Emission for Pixel Fits

Region	Average β	Total Mass $[10^5 M_\odot]$	Average Surface Density $[M_\odot pc^{-2}]$	Average Temperature [K]
1	2.0	230 ± 103	0.5 ± 0.2	24 ± 2
2	2.0	57 ± 19	0.6 ± 0.2	25 ± 1
3	2.0	28 ± 5	0.52 ± 0.09	26.4 ± 0.5
4	2.0	70 ± 22	0.7 ± 0.3	24.4 ± 0.8
5	2.0	42 ± 9	0.34 ± 0.08	22.4 ± 0.8
6	2.0	18 ± 4	0.33 ± 0.08	23.5 ± 0.9
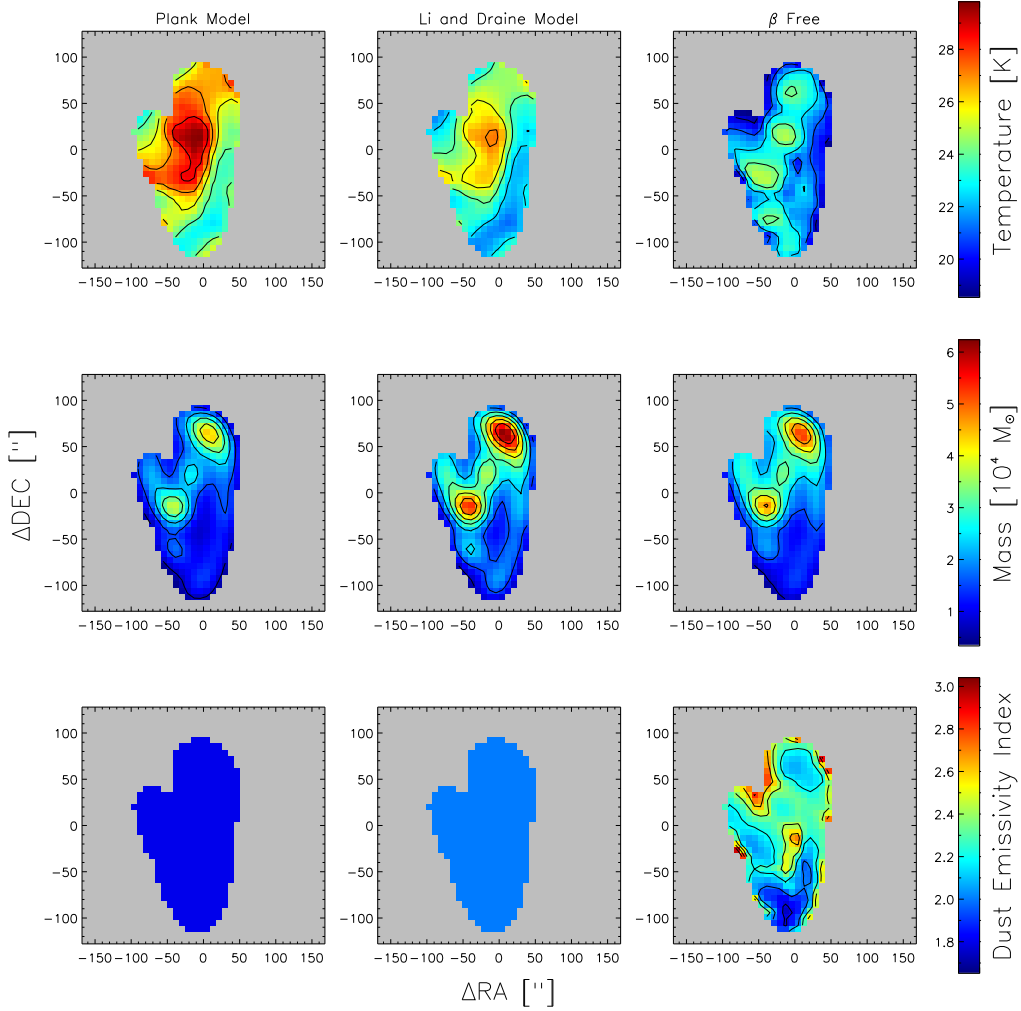
Figure 3.6: Returned value for the SED fits using the 500μm observations with the Planck model in the left column, the Li and Draine model in the middle column, and β as a free variable in the right column. The top row shows the temperature with contours from 19.5K to 28.5K in 1.5K increments. The second row show the returned masses with contours from 1.9$M_\odot$ to 13.3$M_\odot$ in 1.9$M_\odot$ increments. The Li and Draine mass fits have been divided by three to better show the features relative to the other two fits. The bottom row shows the returned dust emissivity index values with contours from 1.8 to 2.8 with 0.2 increments.

Table 3.5.   Best Fit Parameters for β As A Free Parameter Using 500μm
Emission for Pixel Fits

Region	Average β	Total Mass $[10^5 M_\odot]$	Average Surface Density $[10^5 M_\odot pc^{-2}]$	Average Temperature [K]
1	2.2 ± 0.2	73 ± 31	0.14 ± 0.06	22 ± 1
2	2.3 ± 0.2	18 ± 5	0.18 ± 0.05	22 ± 2
3	2.34 ± 0.09	9 ± 1	0.18 ± 0.02	23.0 ± 0.9
4	2.2 ± 0.1	22 ± 5	0.21 ± 0.05	22 ± 1
5	2.1 ± 0.2	12 ± 4	0.10 ± 0.03	22 ± 1
6	2.1 ± 0.1	5 ± 1	0.09 ± 0.03	23.0 ± 0.9

3.2.2 Total Region Flux SED Fits

The second method used to determine the dust mass was to fit the SED to the flux of each region in Figure 3.1. Performing the fit in this manner is beneficial because it increases the signal to noise of the region and produces a more precise set of parameters. Initially, fitting the total flux of each region was carried out in the same fashion as the individual pixel fits by fixing the emissivity index to 1.8 and 2.0, and allowing the emissivity index to vary. This method ran into issues when determining an initial mass to use in the fitting. If we used the same procedure as we did for the pixel fitting, equation 3.4, our initial masses would either converge on a local minimum or to not be able to produce a useable fit. This was due to the Levinberg-Marquardt method not being able to efficiently step through the parameter space to find a useable minimum, or the method would converge to a local minimum instead of the global minimum. The behavior of the fitted parameters with respect to the initial mass is shown in Figure 3.7 for a variable emissivity index.

65

Table 3.6.   Best Fit Parameters for Planck Opacity Using Region Fluxes

Region	β	Mass $[10^5 M_\odot]$	Mean Surface Density $[M_\odot pc^{-2}]$	Temperature [K]
1	2.20 ± 0.03	70 ± 5	0.14 ± 0.01	22.8 ± 0.5
2	2.30 ± 0.03	19 ± 1	0.18 ± 0.01	22.5 ± 0.3
3	2.35 ± 0.03	9.5 ± 0.6	0.21 ± 0.01	23.3 ± 0.3
4	2.30 ± 0.03	23 ± 1	0.22 ± 0.01	22.2 ± 0.2
5	2.00 ± 0.03	11.4 ± 0.8	0.093 ± 0.007	22.3 ± 0.4
6	1.95 ± 0.03	4.6 ± 0.3	0.087 ± 0.006	23.9 ± 0.4

In order to prevent any false convergences, we establish a range of emissivity index values from 1.6 to 2.9 with increments of 0.05 and found the best fit mass and temperature for each of these indices. This method ended up being significantly more robust than allowing the emissivity index to vary. The relationship between the initial mass and the fitted parameters with a fixed emissivity is shown in Figure 3.8, and shows the results are independent of the initial mass up to a cutoff point where the Levinberg-Marquardt method is unable to produce reliable fits. Determining the best emissivity index was decided by which value returned the lowest reduced χ^2 value. The reduced χ^2 and emissivity index plots are shown in Figure 3.9 for each of the regions of NGC3627, where the minimum value is marked by the red line. The best fit results using this method are shown in Table 3.6 using the opacity suggested by the Planck model and the fitted SEDs are shown in Figure 3.10.
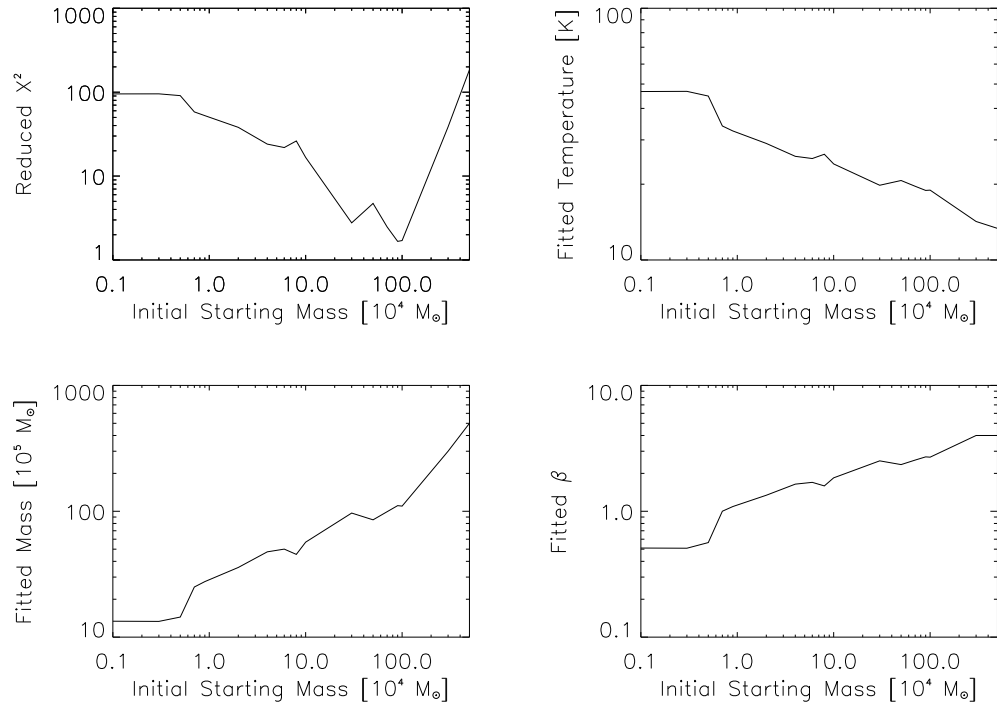
Figure 3.7: Returned SED fitting output with Planck opacity for the χ^2, temperature, mass, and emissivity index with varying initial mass. The top left panels shows the χ^2 values for each starting mass. The top right, bottom left, and bottom right panel show the returned temperatures, mass, and emissivity index.
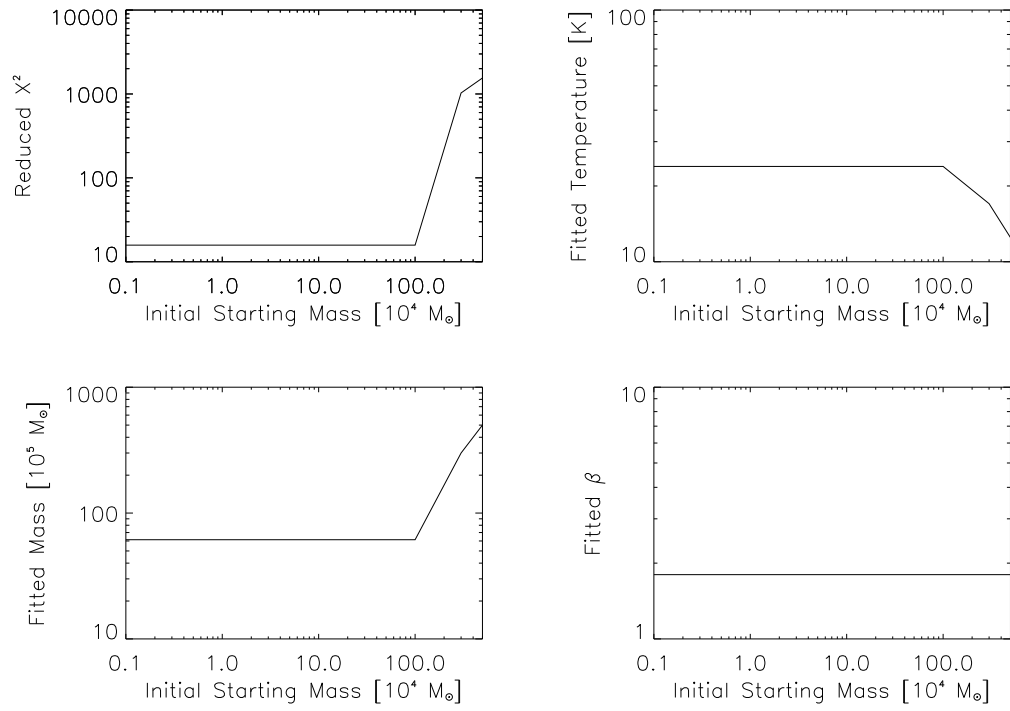
Figure 3.8: The same as figure 3.7, however the emissivity index has been fixed to 1.8.
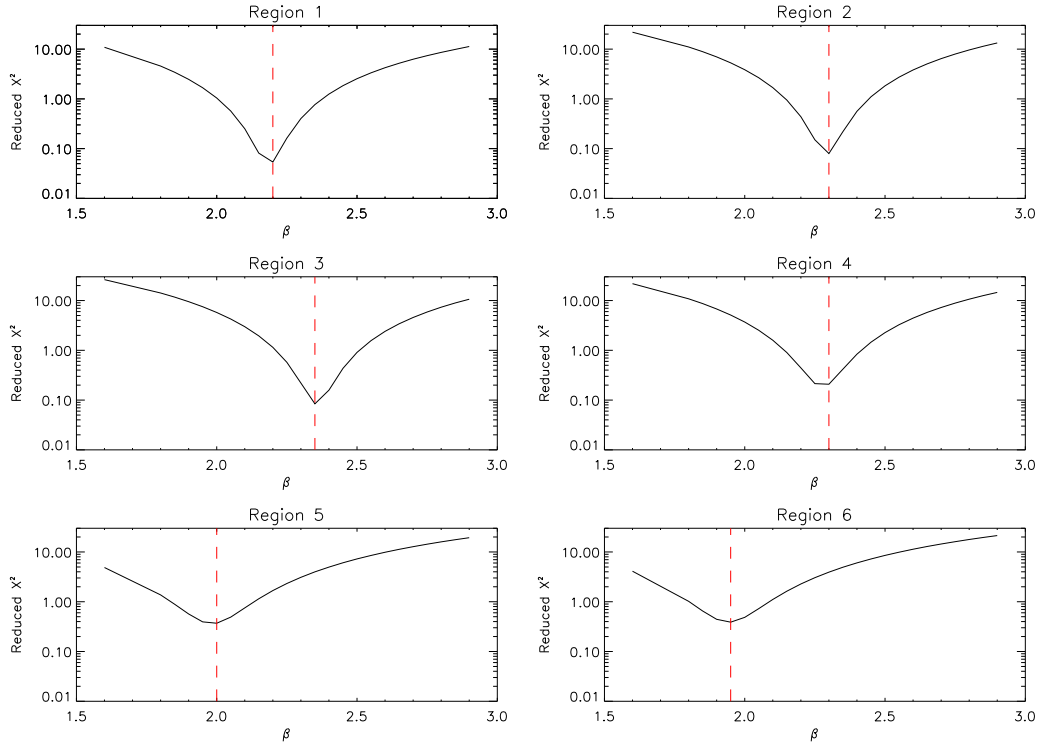
Figure 3.9: Plots for each region from figure 3.1 showing the fixed emissivity index value and the resulting reduced χ^2 value.

(a) Regions 1, 2, and 3 SEDs

(b) Regions 4, 5, and 6 SEDs

Figure 3.10: SED fits for the flux of each region in Figure 3.1 using the Planck Opacity and allowing the emissivity index, β to vary.

3.3 Discussion

3.3.1 Reliability of Individual Pixel Fits

The issue of whether or not the individual pixel fits are reliable for a variable emissivity index is raised after seeing a strong dependence with the initial mass of the region SED fits shown in Figure 3.7. The argument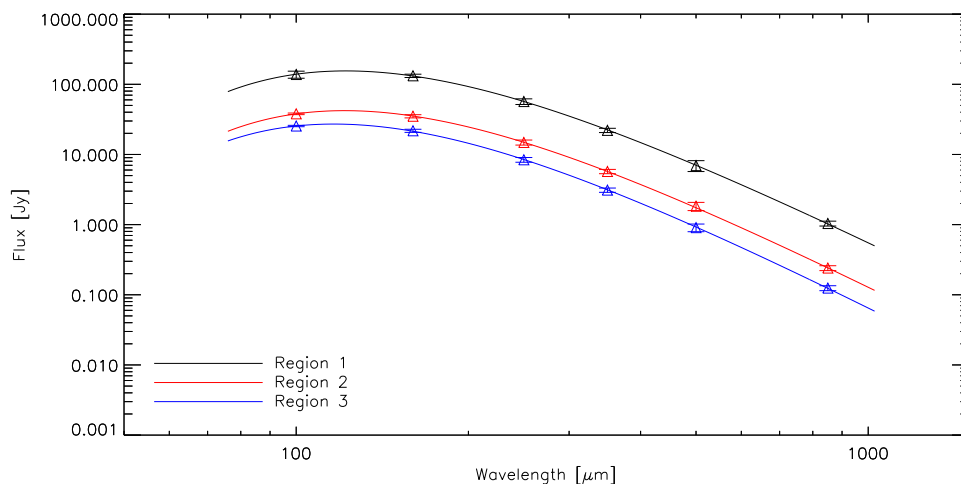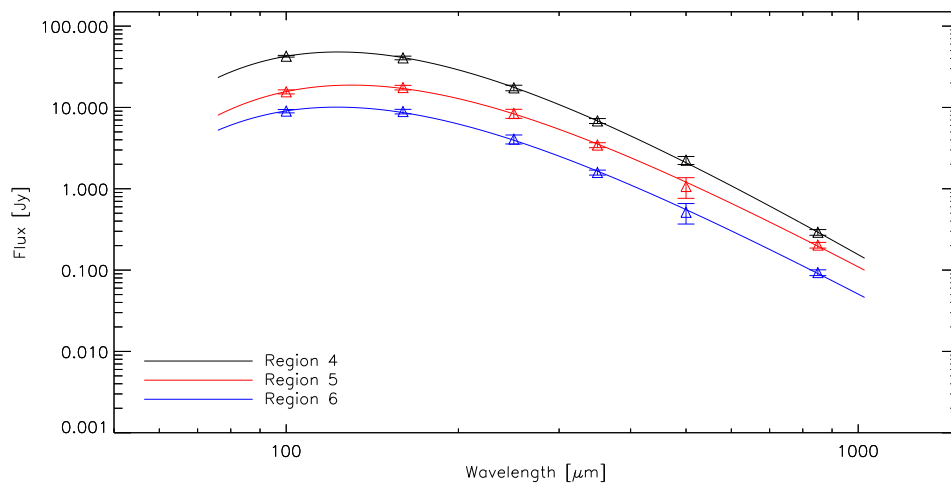 can be made that since both fits have returned the same temperature (T_{pixel}=22±1 K and T_{region}=22.8±0.5 K), emissivity index (β_{pixel}=2.2±0.2 and β_{region}=2.20±0.03), and mass (M_{pixel}=85±38 $M_\odot$ and M_{region}=82±6 $M_\odot$), and the removal of any initial mass dependence for the region fits, the initial values for the pixel fits are able to locate the global minimum of the χ^2 space regardless of any dependence. The inability of the region fits to successfully converge was due to an overestimate of the initial mass. The mass associated with the 250μm flux using the 20K Li and Draine model was scaling the peak of the SED to values larger than what would be expected using the Planck model which is the opacity used for the region fits. The difference between the two initial masses was large enough for the Levinberg-Marquardt method to fail at finding a minimum. This can be remedied by retooling the initial mass to use the Planck model, however by cycling through emissivity index values, we have provided a more reliable check to our pixel maps by breaking the dependency with the initial mass.

3.3.2 Comparison with Previous Work

We can check the validity of our results by comparing them to previous SED fits using the KINGFISH data (Galametz et al., 2012). The best fit parameters from their fitting were T=20.2K±4K and β=2.3±0.2 which agree within error to our results of T=22K±1K and β=2.2±0.2 for a variable emissivity index. To test agreement with our mass we need to take into account several differences in the two analyses. The differences consist of a lessened flux from the extended structure removal, the opacity values used, and which wavelength was used to calculate the mass. The easiest approach to check whether our masses agree is to use the parameters found by Galametz et al. (2012) with our reduced flux. In order to lessen the amount of free parameters we can use the Li and Draine model to calcuate a mass. Using our flux with their fits we get a mass of 276±59×10^5 M$_\odot$ which agrees with the our mass of 230±103×10^5 M$_\odot$.

3.3.3 Effects of 850μm Emission

The major difference between our work on NGC3627 and the work done in Galametz et al. (2012) is the presence of the 850μm data point. In our analysis the presence of the 850μm has been shown to have little effect on the returned parameters. The returned values for a variable emissivity index are shown in table 3.7.

The absence of a significant change in the returned parameters is indicative of a lack of any excess submillimeter emission suggestive of an abundance of a very cold (T $\lesssim$ 10K) dust component (Dale et al., 2012). This excess in emission is typically seen in low-metallicity systems such as dwarf galaxies

Table 3.7.   Best Fit Parameters Excluding 850μm Emission Using Planck
Opacity with Variable Emissivity Index

Region	Average β	Total Mass $[10^5 M_\odot]$	Average Surface Density $[M_\odot pc^{-2}]$	Average Temperature [K]
1	2.3 ± 0.3	75 ± 28	0.15 ± 0.06	22 ± 2
2	2.3 ± 0.3	18 ± 5	0.17 ± 0.05	23 ± 2
3	2.4 ± 0.2	10 ± 1	0.19 ± 0.02	23 ± 1
4	2.2 ± 0.2	22 ± 5	0.21 ± 0.05	23 ± 2
5	2.3 ± 0.2	14 ± 3	0.11 ± 0.03	21 ± 1
6	2.2 ± 0.2	5 ± 1	0.10 ± 0.02	22 ± 1

(Madden et al., 2011). The dwarf galaxies showing an excess typically have a metallicity of $\log(O/H) + 12 \lesssim 8.3$ (Rémy-Ruyer et al., 2013). An 870μm excess has also been seen in NGC3627 (Galametz et al., 2014), but our results show no excess of emission at 850μm (evident in Figures 3.3, 3.4, and 3.5). The discrepancy between our results and Galametz et al. (2014) can be attributed to their treatment of the removal of the CO J=3-2 emission from their date and possibly to how their 870μm data was processed. If their image processing method does not remove extended emission, the submillimeter excess might be attributed to diffuse base. However, we should not expect to see any submillimeter excess given the $\log(O/H) + 12$ is 8.99 for NGC3627 (Moustakas et al., 2010) well above the estimated threshold.

Chapter 4

Dust-to-Gas Ratio and α_{CO}

4.1 Minimizing Scatter Dust-to-Gas Ratio

In order to determine the amount of molecular hydrogen present, we have chosen to use the dust based method to determine a conversion factor. In our analysis we have used the conversion factor α_{CO} which will return the amount of molecular hydrogen present in terms of its surface density. Calculating the amour of molecular hydrogen present with this method involves reducing the scatter of the dust to gas ratio of each pixel. The dust-to-gas ratio is calculated using

$$\delta_{DGR} = \frac{\Sigma_{dust}}{I_{CO} * \alpha_{CO} + \Sigma_{HI}} \qquad (4.1)$$

where δ_{DGR} is the ratio of the surface densities of the dust and gas present in the system, Σ_{dust} is the surface density of the dust in $M_\odot$ pc^{-2}, I_{CO} is the CO intensity in K km s^{-1}, α_{CO} is the conversion factor in units of $M_\odot$ pc^{-2} (K km s^{-1})$^{-1}$, and Σ_{HI} is the surface density of the atomic hydrogen. The scatter

of the dust-to-gas ratio is determined by finding the standard deviation of the pixels assuming a Gaussian distribution.

The ideal configuration was determined using the dust surface densities found in Chapter 3 for the Planck and Li and Draine models. The α_{CO} was handled by assigning it a single value over the range of 0.01 to 100 M$_\odot$ pc^{-2} (K km s^{-1})$^{-1}$, and the best approximated α_{CO} was determined by the lowest resulting dust-to-gas scatter in the pixels of each region in Figure 3.1. A 7th region was added that is the galaxy without the nucleus due to the lack of HI emission in the nucleus of NGC3627. The surface density of molecular hydrogen is then determined by scaling the CO intensity by the calculated conversion factor, and the dust-to-gas ratio is then found by dividing the dust surface density by the sum of the HI and H$_2$ surface densities. The results using Planck model with the CO J=1-0 line are shown in Figure 4.1 where the right panel shows the ratio of H$_2$ to HI against the value of the dust-to-gas ratio in each pixel where the solid red line indicates the mean value for the dust-to-gas ratio and the dotted lines show the variance associated with the configuration. The left panels of Figure 4.1 show the trend of α_{CO} and the scatter in the dust-to-gas ratio. The numerical values of the dust-to-gas ratio, α_{CO}, and H$_2$ surface density using both the Planck and Li and Draine dust masses are shown in Table 4.1. The error on the dust to gas ratio in Table 4.1 is the same as the minimum scatter found.

While CO J=1-0 is the standard molecular tracer of H$_2$ (Bolatto et al., 2013), the observations are not always available. In the situation without CO J=1-0 data an alternative excitation state of CO is used. This was done by
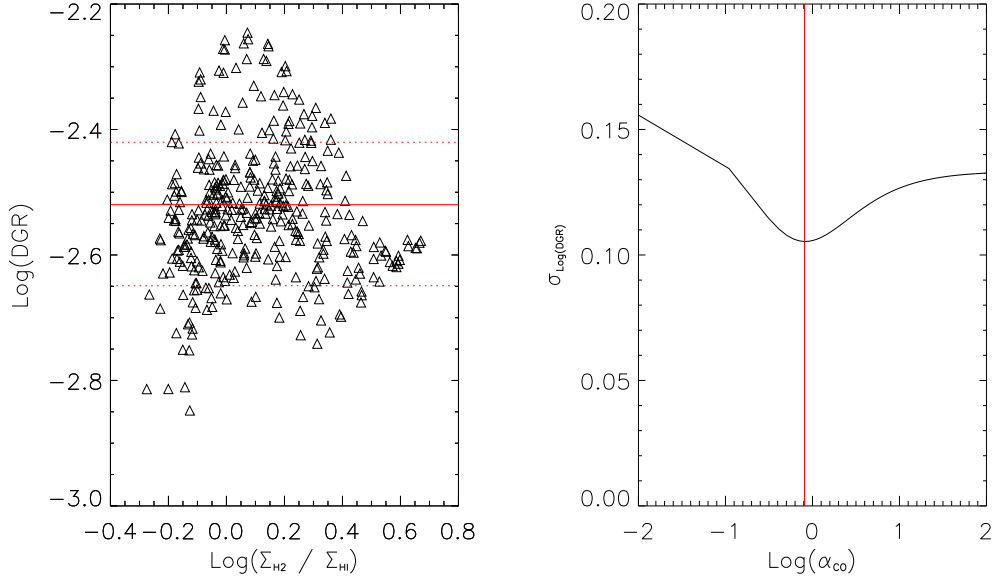
(a) Region 1
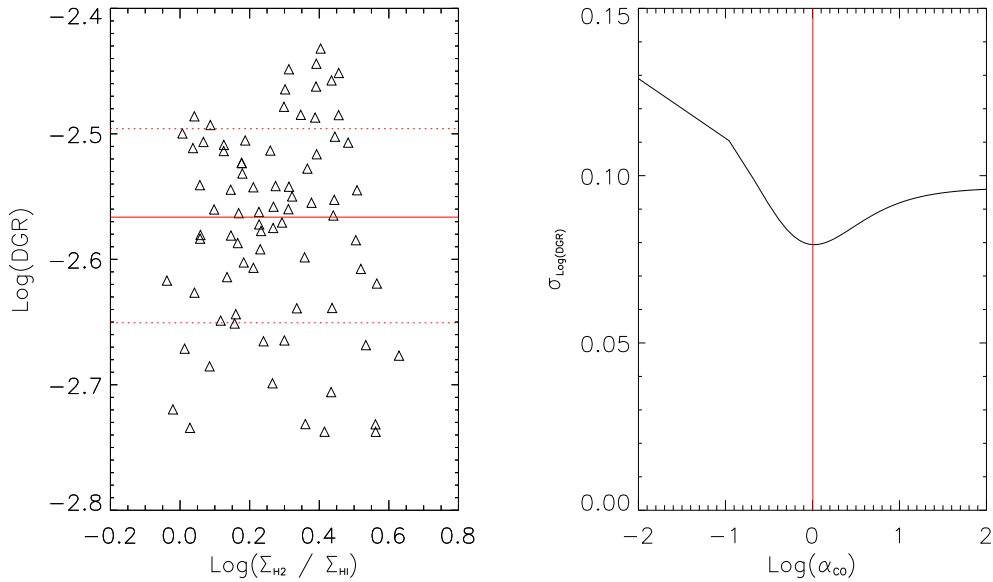
(b) Region 2

Figure 4.1: Plots of the dust-to-gas ratio vs the H₂ to HI surface densities using the calculated α_{CO} and the scatter in the dust-to-gas ratio against the α_{CO} values used. Each were calculated using the CO J=1-0 line.

(c) Region 3

(d) Region 4

Figure 4.1: Plots of the dust-to-gas ratio vs the H_2 to HI surface densities using the calculated α_{CO} and the scatter in the dust-to-gas ratio against the α_{CO} values used. Each were calculated using the CO J=1-0 line.
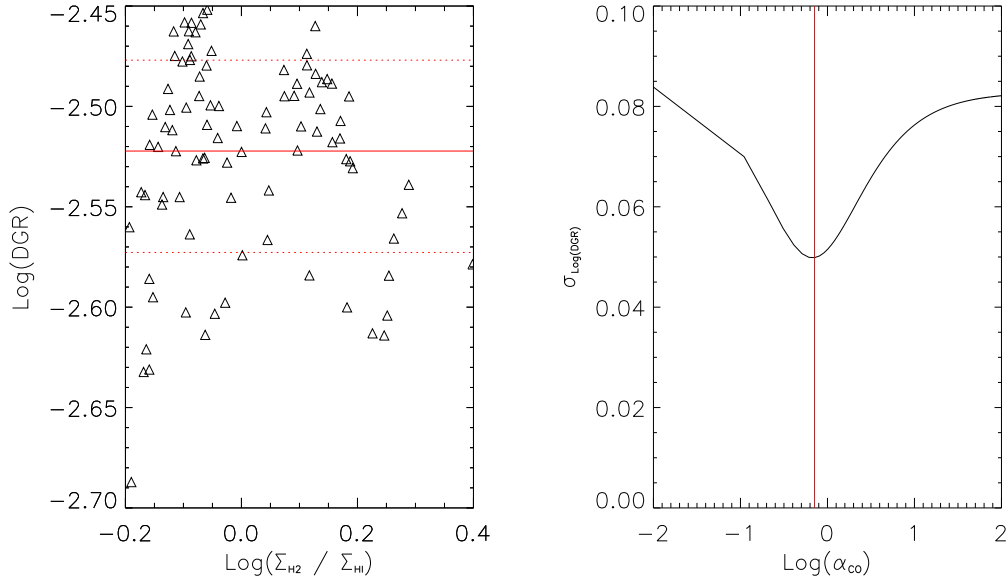
(e) Region 5

(f) Region 6

Figure 4.1: Plots of the dust-to-gas ratio vs the H_2 to HI surface densities using the calculated α_{CO} and the scatter in the dust-to-gas ratio against the α_{CO} values used. Each were calculated using the CO J=1-0 line.
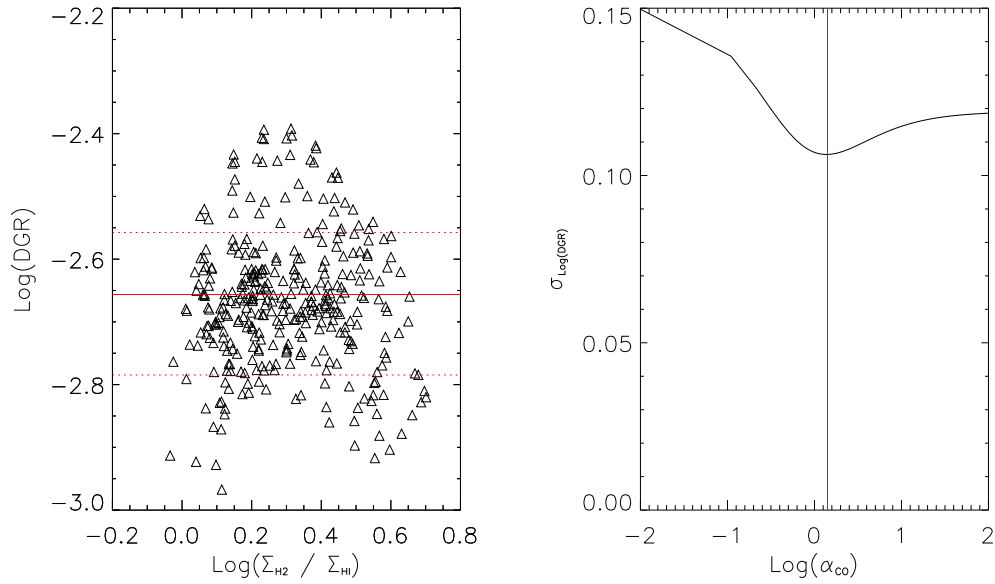
(g) Region 1 Without the Nucleus
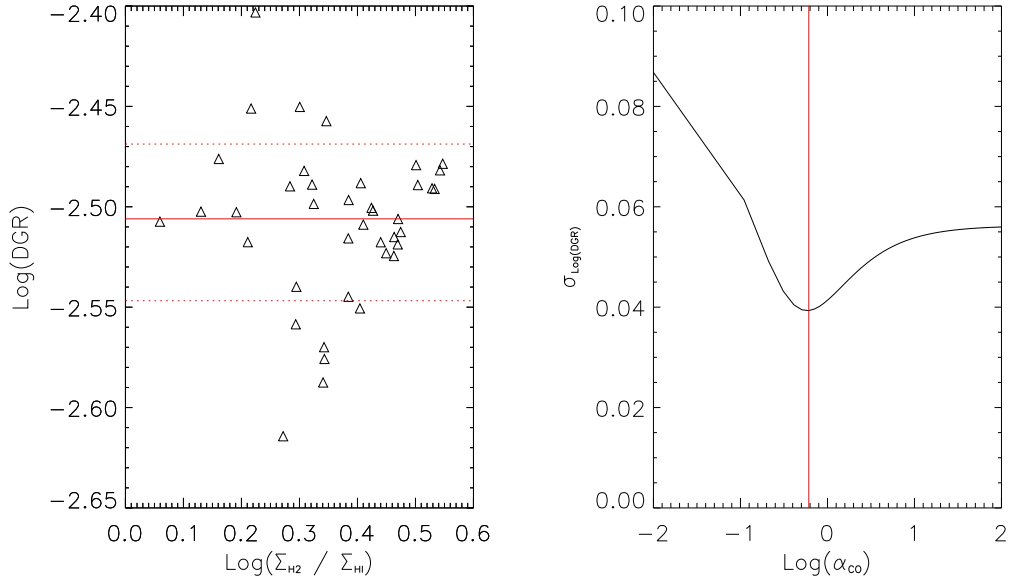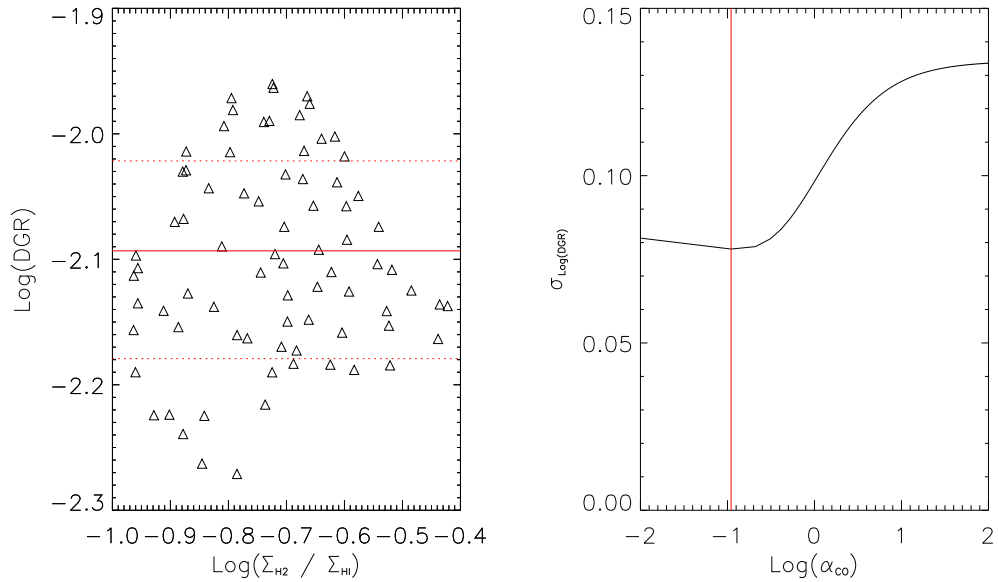
Figure 4.1: Plots of the dust-to-gas ratio vs the H_2 to HI surface densities using the calculated α_{CO} and the scatter in the dust-to-gas ratio against the α_{CO} values used. Each were calculated using the CO J=1-0 line.
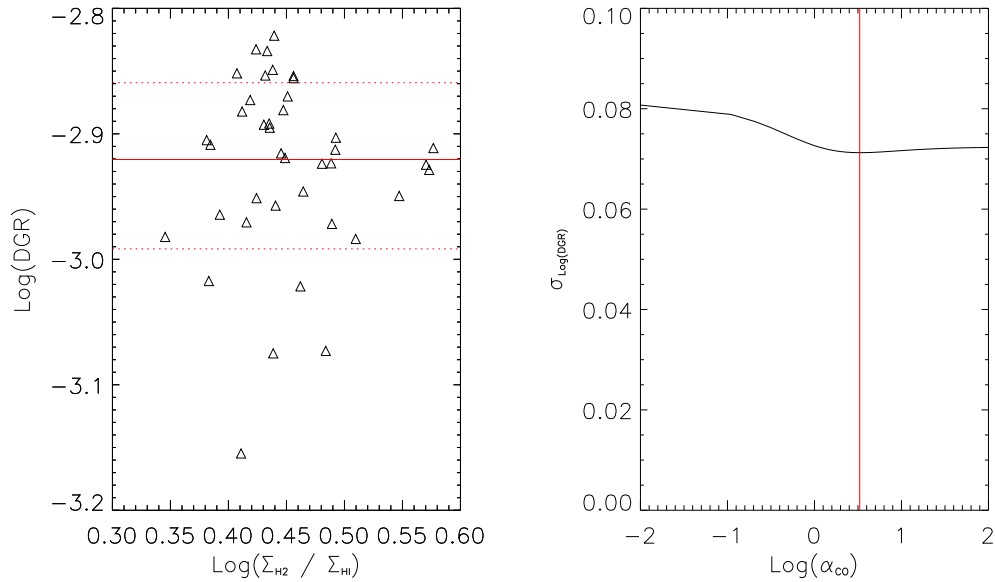
Table 4.1.   Dust-to-gas ratio, α_{CO}, and H$_2$ Surface Density using CO J=1-0 Tracer

Opacity Model	Dust-to-Gas Ratio	α_{CO} [M$_\odot$ pc^{-2} (K km s^{-1})$^{-1}$]	Average Σ_{H_2} per Pixel [M$_\odot$ pc^{-2}]
Region 1			
Planck	0.017 ± 0.004	0.21 ± 0.05	4 ± 2
Li and Draine	0.07 ± 0.02	0.21 ± 0.05	4 ± 2
Region 2			
Planck	0.012 ± 0.002	0.31 ± 0.05	8 ± 2
Li and Draine	0.05 ± 0.01	0.31 ± 0.05	8 ± 3
Region 3			
Planck	0.025 ± 0.003	0.11 ± 0.05	4.1 ± 0.9
Li and Draine	0.11 ± 0.01	0.11 ± 0.05	4.1 ± 0.9
Region 4			
Planck	0.028 ± 0.004	0.11 ± 0.05	3 ± 1
Li and Draine	0.12 ± 0.02	0.11 ± 0.05	3 ± 1
Region 5			
Planck	0.023 ± 0.004	0.11 ± 0.05	1.5 ± 0.7
Li and Draine	0.10 ± 0.02	0.11 ± 0.05	1.5 ± 0.7
Region 6			
Planck	0.009 ± 0.001	0.61 ± 0.05	6 ± 1
Li and Draine	0.040 ± 0.006	0.61 ± 0.05	6 ± 1
No Nucleus			
Planck	0.018 ± 0.004	0.21 ± 0.05	4 ± 2
Li and Draine	0.08 ± 0.02	0.21 ± 0.05	4 ± 2

Sandstrom et al. (2013) using the CO J=2-1 transition, and by Warren et al. (2010) using the CO J=3-2 transition, where the observations were scaled to the expected intensity of the CO J=1-0 using a line ratio. We have found the line ratio of the 2-1/1-0 to be 0.39 for the galaxy on a whole, and can examine the effects of using this technique to approximate the CO J=1-0 transition in this method. The results for the dust-to-gas ratio, α_{CO}, and H_2 surface density are shown in Table 4.2.

Table 4.2.   Dust-to-gas ratio, α_{CO}, and H$_2$ Surface Density using CO J=2-1 Tracer

Opacity Model	Dust-to-Gas Ratio	α_{CO} [M$_\odot$ pc^{-2} (K km s^{-1})$^{-1}$]	Average Σ_{H_2} per Pixel [M$_\odot$ pc^{-2}]
Region 1			
Planck	0.058 ± 0.009	0.31 ± 0.05	6 ± 4
Li and Draine	0.017 ± 0.003	0.21 ± 0.05	4 ± 2
Region 2			
Planck	0.056 ± 0.003	0.31 ± 0.05	8 ± 3
Li and Draine	0.013 ± 0.001	0.31 ± 0.05	8 ± 3
Region 3			
Planck	0.13 ± 0.01	0.11 ± 0.05	4 ± 1
Li and Draine	0.029 ± 0.003	0.11 ± 0.05	4 ± 1
Region 4			
Planck	0.045 ± 0.009	0.31 ± 0.05	12 ± 4
Li and Draine	0.010 ± 0.001	0.41 ± 0.05	12 ± 4
Region 5			
Planck	0.049 ± 0.007	0.41 ± 0.05	5 ± 2
Li and Draine	0.014 ± 0.002	0.31 ± 0.05	4 ± 1
Region 6			
Planck	0.043 ± 0.003	0.51 ± 0.05	5 ± 2
Li and Draine	0.011 ± 0.001	0.41 ± 0.05	4 ± 1
No Nucleus			
Planck	0.043 ± 0.003	0.31 ± 0.05	6 ± 3
Li and Draine	0.013 ± 0.002	0.31 ± 0.05	6 ± 3

Bibliography

Abel, T., Anninos, P., Zhang, Y., & Norman, M. L. 1997, New A, 2, 181

Abergel, A., Ade, P. A. R., Aghanim, N., Alves, M. I. R., Aniano, G., Armitage-Caplan, C., Arnaud, M., Ashdown, M., Atrio-Barandela, F., Aumont, J., & et al. 2013, ArXiv e-prints

Barrett, A. H. 1964, Nature, 202, 475

Bolatto, A. D., Wolfire, M., & Leroy, A. K. 2013, ARA&A, 51, 207

Boulanger, F., Abergel, A., Bernard, J.-P., Burton, W. B., Desert, F.-X., Hartmann, D., Lagache, G., & Puget, J.-L. 1996, A&A, 312, 256

Burden, R. L. & Faires, J. D. 2001, Numerical analysis

Calzetti, D., Wu, S.-Y., Hong, S., Kennicutt, R. C., Lee, J. C., Dale, D. A., Engelbracht, C. W., van Zee, L., Draine, B. T., Hao, C.-N., Gordon, K. D., Moustakas, J., Murphy, E. J., Regan, M., Begum, A., Block, M., Dalcanton, J., Funes, J., Gil de Paz, A., Johnson, B., Sakai, S., Skillman, E., Walter, F., Weisz, D., Williams, B., & Wu, Y. 2010, ApJ, 714, 1256

Chapin, E. L., Berry, D. S., Gibb, A. G., Jenness, T., Scott, D., Tilanus, R. P. J., Economou, F., & Holland, W. S. 2013, MNRAS, 430, 2545

Dale, D. A., Aniano, G., Engelbracht, C. W., Hinz, J. L., Krause, O., Montiel, E. J., Roussel, H., Appleton, P. N., Armus, L., Beirão, P., Bolatto, A. D.,

Brandl, B. R., Calzetti, D., Crocker, A. F., Croxall, K. V., Draine, B. T., Galametz, M., Gordon, K. D., Groves, B. A., Hao, C.-N., Helou, G., Hunt, L. K., Johnson, B. D., Kennicutt, R. C., Koda, J., Leroy, A. K., Li, Y., Meidt, S. E., Miller, A. E., Murphy, E. J., Rahman, N., Rix, H.-W., Sandstrom, K. M., Sauvage, M., Schinnerer, E., Skibba, R. A., Smith, J.-D. T., Tabatabaei, F. S., Walter, F., Wilson, C. D., Wolfire, M. G., & Zibetti, S. 2012, ApJ, 745, 95

Dempsey, J. T., Friberg, P., Jenness, T., Tilanus, R. P. J., Thomas, H. S., Holland, W. S., Bintley, D., Berry, D. S., Chapin, E. L., Chrysostomou, A., Davis, G. R., Gibb, A. G., Parsons, H., & Robson, E. I. 2013, MNRAS, 430, 2534

Dobbs, C. L., Krumholz, M. R., Ballesteros-Paredes, J., Bolatto, A. D., Fukui, Y., Heyer, M., Mac Low, M.-M., Ostriker, E. C., & Vázquez-Semadeni, E. 2013, ArXiv e-prints

Drabek, E., Hatchell, J., Friberg, P., Richer, J., Graves, S., Buckle, J. V., Nutter, D., Johnstone, D., & Di Francesco, J. 2012, MNRAS, 426, 23

Draine, B. T. 2011, Physics of the Interstellar and Intergalactic Medium

Draine, B. T., Dale, D. A., Bendo, G., Gordon, K. D., Smith, J. D. T., Armus, L., Engelbracht, C. W., Helou, G., Kennicutt, Jr., R. C., Li, A., Roussel, H., Walter, F., Calzetti, D., Moustakas, J., Murphy, E. J., Rieke, G. H., Bot, C., Hollenbach, D. J., Sheth, K., & Teplitz, H. I. 2007, ApJ, 663, 866

Dumke, M., Krause, M., Beck, R., Soida, M., Urbanik, M., & Wielebinski, R. 2011, in Astronomical Society of the Pacific Conference Series, Vol.

446, Galaxy Evolution: Infrared to Millimeter Wavelength Perspective, ed. W. Wang, J. Lu, Z. Luo, Z. Yang, H. Hua, & Z. Chen, 111

Elmegreen, B. G. 1987, ApJ, 312, 626

Field, G. B. & Saslaw, W. C. 1965, ApJ, 142, 568

Freedman, W. L., Madore, B. F., Gibson, B. K., Ferrarese, L., Kelson, D. D., Sakai, S., Mould, J. R., Kennicutt, Jr., R. C., Ford, H. C., Graham, J. A., Huchra, J. P., Hughes, S. M. G., Illingworth, G. D., Macri, L. M., & Stetson, P. B. 2001, ApJ, 553, 47

Galametz, M., Albrecht, M., Kennicutt, R., Aniano, G., Bertoldi, F., Calzetti, D., Croxall, K. V., Dale, D., Draine, B., Engelbracht, C., Gordon, K., Hinz, J., Hunt, L. K., Kirkpatrick, A., Murphy, E., Roussel, H., Skibba, R. A., Walter, F., Weiss, A., & Wilson, C. D. 2014, MNRAS, 439, 2542

Galametz, M., Kennicutt, R. C., Albrecht, M., Aniano, G., Armus, L., Bertoldi, F., Calzetti, D., Crocker, A. F., Croxall, K. V., Dale, D. A., Donovan Meyer, J., Draine, B. T., Engelbracht, C. W., Hinz, J. L., Roussel, H., Skibba, R. A., Tabatabaei, F. S., Walter, F., Weiss, A., Wilson, C. D., & Wolfire, M. G. 2012, MNRAS, 425, 763

Gavin, H. P. 2013, The Levenberg-Marquardt method for nonlinear least squares curve-fitting problems, Tech. rep., Department of Civil and Environmental Engineering, Duke University

Glover, S. C. O. 2003, ApJ, 584, 331

Gould, R. J. & Salpeter, E. E. 1963, ApJ, 138, 393

Gry, C., Boulanger, F., Nehmé, C., Pineau des Forêts, G., Habart, E., & Falgarone, E. 2002, A&A, 391, 675

Haynes, M. P., Giovanelli, R., & Roberts, M. S. 1979, ApJ, 229, 83

Herbst, E., Chang, Q., & Cuppen, H. M. 2005, Journal of Physics Conference Series, 6, 18

Hildebrand, R. H. 1983, QJRAS, 24, 267

Holland, W. S., Bintley, D., Chapin, E. L., Chrysostomou, A., Davis, G. R., Dempsey, J. T., Duncan, W. D., Fich, M., Friberg, P., Halpern, M., Irwin, K. D., Jenness, T., Kelly, B. D., MacIntosh, M. J., Robson, E. I., Scott, D., Ade, P. A. R., Atad-Ettedgui, E., Berry, D. S., Craig, S. C., Gao, X., Gibb, A. G., Hilton, G. C., Hollister, M. I., Kycia, J. B., Lunney, D. W., McGregor, H., Montgomery, D., Parkes, W., Tilanus, R. P. J., Ullom, J. N., Walther, C. A., Walton, A. J., Woodcraft, A. L., Amiri, M., Atkinson, D., Burger, B., Chuter, T., Coulson, I. M., Doriese, W. B., Dunare, C., Economou, F., Niemack, M. D., Parsons, H. A. L., Reintsema, C. D., Sibthorpe, B., Smail, I., Sudiwala, R., & Thomas, H. S. 2013, MNRAS, 430, 2513

Israel, F. P., Bontekoe, T. R., & Kester, D. J. M. 1996, A&A, 308, 723

Jura, M. 1975, ApJ, 197, 575

Kennicutt, R. C., Calzetti, D., Aniano, G., Appleton, P., Armus, L., Beirão, P., Bolatto, A. D., Brandl, B., Crocker, A., Croxall, K., Dale, D. A., Meyer, J. D., Draine, B. T., Engelbracht, C. W., Galametz, M., Gordon, K. D., Groves, B., Hao, C.-N., Helou, G., Hinz, J., Hunt, L. K., Johnson, B.,

Koda, J., Krause, O., Leroy, A. K., Li, Y., Meidt, S., Montiel, E., Murphy, E. J., Rahman, N., Rix, H.-W., Roussel, H., Sandstrom, K., Sauvage, M., Schinnerer, E., Skibba, R., Smith, J. D. T., Srinivasan, S., Vigroux, L., Walter, F., Wilson, C. D., Wolfire, M., & Zibetti, S. 2011, PASP, 123, 1347

Kennicutt, R. C. & Evans, N. J. 2012, ARA&A, 50, 531

Kennicutt, Jr., R. C., Armus, L., Bendo, G., Calzetti, D., Dale, D. A., Draine, B. T., Engelbracht, C. W., Gordon, K. D., Grauer, A. D., Helou, G., Hollenbach, D. J., Jarrett, T. H., Kewley, L. J., Leitherer, C., Li, A., Malhotra, S., Regan, M. W., Rieke, G. H., Rieke, M. J., Roussel, H., Smith, J.-D. T., Thornley, M. D., & Walter, F. 2003, PASP, 115, 928

Kim, W.-T. & Ostriker, E. C. 2001, ApJ, 559, 70

Krumholz, M. R. 2014, ArXiv e-prints

Kuno, N., Sato, N., Nakanishi, H., Hirota, A., Tosaki, T., Shioya, Y., Sorai, K., Nakai, N., Nishiyama, K., & Vila-Vilaró, B. 2007, PASJ, 59, 117

Kwan, J. 1979, ApJ, 229, 567

Leroy, A. K., Bolatto, A., Gordon, K., Sandstrom, K., Gratier, P., Rosolowsky, E., Engelbracht, C. W., Mizuno, N., Corbelli, E., Fukui, Y., & Kawamura, A. 2011, ApJ, 737, 12

Leroy, A. K., Walter, F., Bigiel, F., Usero, A., Weiss, A., Brinks, E., de Blok, W. J. G., Kennicutt, R. C., Schuster, K.-F., Kramer, C., Wiesemeyer, H. W., & Roussel, H. 2009, AJ, 137, 4670

87

Li, A. 2005, in American Institute of Physics Conference Series, Vol. 761, The Spectral Energy Distributions of Gas-Rich Galaxies: Confronting Models with Data, ed. C. C. Popescu & R. J. Tuffs, 123–133

Li, A. & Draine, B. T. 2001, ApJ, 554, 778

Madden, S. C., Galametz, M., Cormier, D., Lebouteiller, V., Galliano, F., Hony, S., Rémy, A., Sauvage, M., Contursi, A., Sturm, E., Poglitsch, A., Pohlen, M., Smith, M. W. L., Bendo, G., & O'Halloran, B. 2011, in EAS Publications Series, Vol. 52, EAS Publications Series, ed. M. Röllig, R. Simon, V. Ossenkopf, & J. Stutzki, 95–101

Madden, S. C., Poglitsch, A., Geis, N., Stacey, G. J., & Townes, C. H. 1997, ApJ, 483, 200

Markwardt, C. B. 2009, in Astronomical Society of the Pacific Conference Series, Vol. 411, Astronomical Data Analysis Software and Systems XVIII, ed. D. A. Bohlender, D. Durand, & P. Dowler, 251

McKee, C. F. & Ostriker, E. C. 2007, ARA&A, 45, 565

Moustakas, J., Kennicutt, Jr., R. C., Tremonti, C. A., Dale, D. A., Smith, J.-D. T., & Calzetti, D. 2010, ApJS, 190, 233

Palla, F., Salpeter, E. E., & Stahler, S. W. 1983, ApJ, 271, 632

Parker, E. N. 1966, ApJ, 145, 811

Pirronello, V., Liu, C., Shen, L., & Vidali, G. 1997, ApJ, 475, L69

Planck Collaboration, Abergel, A., Ade, P. A. R., Aghanim, N., Arnaud, M., Ashdown, M., Aumont, J., Baccigalupi, C., Balbi, A., Banday, A. J., Barreiro, R. B., Bartlett, J. G., Battaner, E., Benabed, K., Benoît, A., Bernard, J.-P., Bersanelli, M., Bhatia, R., Bock, J. J., Bonaldi, A., Bond, J. R., Borrill, J., Bouchet, F. R., Boulanger, F., Bucher, M., Burigana, C., Cabella, P., Cardoso, J.-F., Catalano, A., Cayón, L., Challinor, A., Chamballu, A., Chiang, L.-Y., Chiang, C., Christensen, P. R., Clements, D. L., Colombi, S., Couchot, F., Coulais, A., Crill, B. P., Cuttaia, F., Danese, L., Davies, R. D., Davis, R. J., de Bernardis, P., de Gasperis, G., de Rosa, A., de Zotti, G., Delabrouille, J., Delouis, J.-M., Désert, F.-X., Dickinson, C., Dobashi, K., Donzelli, S., Doré, O., Dörl, U., Douspis, M., Dupac, X., Efstathiou, G., Enßlin, T. A., Eriksen, H. K., Finelli, F., Forni, O., Frailis, M., Franceschi, E., Galeotta, S., Ganga, K., Giard, M., Giardino, G., Giraud-Héraud, Y., González-Nuevo, J., Górski, K. M., Gratton, S., Gregorio, A., Gruppuso, A., Guillet, V., Hansen, F. K., Harrison, D., Henrot-Versillé, S., Herranz, D., Hildebrandt, S. R., Hivon, E., Hobson, M., Holmes, W. A., Hovest, W., Hoyland, R. J., Huffenberger, K. M., Jaffe, A. H., Jones, A., Jones, W. C., Juvela, M., Keihänen, E., Keskitalo, R., Kisner, T. S., Kneissl, R., Knox, L., Kurki-Suonio, H., Lagache, G., Lamarre, J.-M., Lasenby, A., Laureijs, R. J., Lawrence, C. R., Leach, S., Leonardi, R., Leroy, C., Linden-Vørnle, M., López-Caniego, M., Lubin, P. M., Macías-Pérez, J. F., MacTavish, C. J., Maffei, B., Mandolesi, N., Mann, R., Maris, M., Marshall, D. J., Martin, P., Martínez-González, E., Masi, S., Matarrese, S., Matthai, F., Mazzotta, P., McGehee, P., Meinhold, P. R., Melchiorri, A., Mendes, L., Mennella, A., Mitra, S., Miville-Deschênes, M.-A., Moneti, A., Montier, L., Morgante, G.,

Mortlock, D., Munshi, D., Murphy, A., Naselsky, P., Natoli, P., Netterfield, C. B., Nørgaard-Nielsen, H. U., Noviello, F., Novikov, D., Novikov, I., Osborne, S., Pajot, F., Paladini, R., Pasian, F., Patanchon, G., Perdereau, O., Perotto, L., Perrotta, F., Piacentini, F., Piat, M., Plaszczynski, S., Pointecouteau, E., Polenta, G., Ponthieu, N., Poutanen, T., Prézeau, G., Prunet, S., Puget, J.-L., Reach, W. T., Rebolo, R., Reinecke, M., Renault, C., Ricciardi, S., Riller, T., Ristorcelli, I., Rocha, G., Rosset, C., Rubiño-Martín, J. A., Rusholme, B., Sandri, M., Santos, D., Savini, G., Scott, D., Seiffert, M. D., Shellard, P., Smoot, G. F., Starck, J.-L., Stivoli, F., Stolyarov, V., Sudiwala, R., Sygnet, J.-F., Tauber, J. A., Terenzi, L., Toffolatti, L., Tomasi, M., Torre, J.-P., Tristram, M., Tuovinen, J., Umana, G., Valenziano, L., Verstraete, L., Vielva, P., Villa, F., Vittorio, N., Wade, L. A., Wandelt, B. D., Yvon, D., Zacchei, A., & Zonca, A. 2011, A&A, 536, A25

Rémy-Ruyer, A., Madden, S. C., Galliano, F., Hony, S., Sauvage, M., Bendo, G. J., Roussel, H., Pohlen, M., Smith, M. W. L., Galametz, M., Cormier, D., Lebouteiller, V., Wu, R., Baes, M., Barlow, M. J., Boquien, M., Boselli, A., Ciesla, L., De Looze, I., Karczewski, O. Ł., Panuzzo, P., Spinoglio, L., Vaccari, M., & Wilson, C. D. 2013, A&A, 557, A95

Reuter, H.-P., Sievers, A. W., Pohl, M., Lesch, H., & Wielebinski, R. 1996, A&A, 306, 721

Rosenberg, M. J. F., Kazandjian, M. V., van der Werf, P. P., Israel, F. P., Meijerink, R., Weiß, A., Requena-Torres, M. A., & Güsten, R. 2014, A&A, 564, A126

Rots, A. H. 1978, AJ, 83, 219

Rybicki, G. B. & Lightman, A. P. 1986, Radiative Processes in Astrophysics

Sandstrom, K. M., Leroy, A. K., Walter, F., Bolatto, A. D., Croxall, K. V.,
    Draine, B. T., Wilson, C. D., Wolfire, M., Calzetti, D., Kennicutt, R. C.,
    Aniano, G., Donovan Meyer, J., Usero, A., Bigiel, F., Brinks, E., de Blok,
    W. J. G., Crocker, A., Dale, D., Engelbracht, C. W., Galametz, M., Groves,
    B., Hunt, L. K., Koda, J., Kreckel, K., Linz, H., Meidt, S., Pellegrini,
    E., Rix, H.-W., Roussel, H., Schinnerer, E., Schruba, A., Schuster, K.-F.,
    Skibba, R., van der Laan, T., Appleton, P., Armus, L., Brandl, B., Gordon,
    K., Hinz, J., Krause, O., Montiel, E., Sauvage, M., Schmiedeke, A., Smith,
    J. D. T., & Vigroux, L. 2013, ApJ, 777, 5

Skibba, R. A., Engelbracht, C. W., Dale, D., Hinz, J., Zibetti, S., Crocker, A.,
    Groves, B., Hunt, L., Johnson, B. D., Meidt, S., Murphy, E., Appleton, P.,
    Armus, L., Bolatto, A., Brandl, B., Calzetti, D., Croxall, K., Galametz, M.,
    Gordon, K. D., Kennicutt, R. C., Koda, J., Krause, O., Montiel, E., Rix,
    H.-W., Roussel, H., Sandstrom, K., Sauvage, M., Schinnerer, E., Smith,
    J. D., Walter, F., Wilson, C. D., & Wolfire, M. 2011, ApJ, 738, 89

Soida, M., Urbanik, M., Beck, R., Wielebinski, R., & Balkowski, C. 2001,
    A&A, 378, 40

Tabatabaei, F. S., Braine, J., Xilouris, E. M., Kramer, C., Boquien, M.,
    Combes, F., Henkel, C., Relano, M., Verley, S., Gratier, P., Israel, F., Wied-
    ner, M. C., Röllig, M., Schuster, K. F., & van der Werf, P. 2014, A&A, 561,
    A95

Walcher, J., Groves, B., Budavári, T., & Dale, D. 2011, Ap&SS, 331, 1

Walter, F., Brinks, E., de Blok, W. J. G., Bigiel, F., Kennicutt, Jr., R. C., Thornley, M. D., & Leroy, A. 2008, AJ, 136, 2563

Warren, B. E., Wilson, C. D., Israel, F. P., Serjeant, S., Bendo, G. J., Brinks, E., Clements, D. L., Irwin, J. A., Knapen, J. H., Leech, J., Matthews, H. E., Mühle, S., Mortimer, A. M. J., Petitpas, G., Sinukoff, E., Spekkens, K., Tan, B. K., Tilanus, R. P. J., Usero, A., van der Werf, P. P., Vlahakis, C., Wiegert, T., & Zhu, M. 2010, ApJ, 714, 571

Watanabe, Y., Sorai, K., Kuno, N., & Habe, A. 2011, MNRAS, 411, 1409

Wilson, C. D., Warren, B. E., Israel, F. P., Serjeant, S., Attewell, D., Bendo, G. J., Butner, H. M., Chanial, P., Clements, D. L., Golding, J., Heesen, V., Irwin, J., Leech, J., Matthews, H. E., Mühle, S., Mortier, A. M. J., Petitpas, G., Sánchez-Gallego, J. R., Sinukoff, E., Shorten, K., Tan, B. K., Tilanus, R. P. J., Usero, A., Vaccari, M., Wiegert, T., Zhu, M., Alexander, D. M., Alexander, P., Azimlu, M., Barmby, P., Brar, R., Bridge, C., Brinks, E., Brooks, S., Coppin, K., Côté, S., Côté, P., Courteau, S., Davies, J., Eales, S., Fich, M., Hudson, M., Hughes, D. H., Ivison, R. J., Knapen, J. H., Page, M., Parkin, T. J., Rigopoulou, D., Rosolowsky, E., Seaquist, E. R., Spekkens, K., Tanvir, N., van der Hulst, J. M., van der Werf, P., Vlahakis, C., Webb, T. M., Weferling, B., & White, G. J. 2012, MNRAS, 424, 3050

Wolfire, M. G., McKee, C. F., Hollenbach, D., & Tielens, A. G. G. M. 2003, ApJ, 587, 278

Wolfire, M. G., Tielens, A. G. G. M., Hollenbach, D., & Kaufman, M. J. 2008, ApJ, 680, 384